Modeling fracture in polymeric material using phase field method based on critical stretch criterion

P. Aurojyoti [*], A. Rajagopal, K.S.S. Reddy

Department of Civil Engineering, IIT Hyderabad, India

A R T I C L E   I N F O

A B S T R A C T

In this work, the phase field method (PFM) is applied for modeling fracture in the polymeric type of materials. Considering the large extensibility of polymer chains before fracture, a crack initiation criteria based on a critical stretch value is proposed. The tensile stretches in the material contribute to the active strain energy, which is responsible for driving fracture. Additive decomposition of strain energy into active and passive parts is adopted based on the critical stretch value of polymer chains in a phase-field setting. This critical value is determined by assuming an equivalent uniaxial tensile state of stress in front of the crack tip at the onset of fracture. The stretch of individual polymeric chains is determined by using a polymer network model. The critical fracture toughness of the polymer is kept constant up to the onset of fracture and a gradually reducing value of it is adopted in front of the crack tip beyond the critical stretch. A hybrid phase-field formulation with a staggered solver is used owing to its numerical efficiency and robustness. The effectiveness and applicability of the present model are demonstrated through various numerical examples.

1. Introduction

Hyperelastic materials such as rubber, hydrogels, elastomers, textile fabrics, shape memory polymers are vastly used in various modern engineering applications. These types of materials have relatively more desirable mechanical properties (heat resistance, stretchability, strength) and behave elastically at large strain. Specifically, rubber has high deformability and dissipative property, due to which it is widely used in damping applications Coveney (2006), sealants (Syao and Malysheva, 2014), etc. Other industrial applications of it includes tyres, gaskets in automotive, aviation industry, and spaceships. Using various mathematical tools and computational framework, researchers have been trying to find the true behavior of hyperelastic materials (Fu et al., 2020; Basak et al., 2021; He et al., 2022).

Understanding the mechanical behavior, more importantly, damage and fracture in rubber-like materials is an indispensable area among researchers. Most rubber-like incompressible polymers are best represented by a network structure of polymer chains. In such materials, the 8-chain network model proposed by Arruda and Boyce (1993) is found to predict results close to the experimental results than the 3-chain, 4-chain, and full network model (Wu and Van Der Giessen, 1993). These micro-mechanically motivated models capture the behavior of polymer chains at the microscopic scale and are able to represent it on the continuum scale by the use of a representative volume element (RVE). A detailed description of different phenomenological and micro-mechanical constitutive models for rubber-like materials and polymers is given in Hossain and Steinmann (2013). The state of the art in isotropic hyperelasticity constitutive models for rubber like materials is given in Dal et al. (2021). Failure phenomena in certain class of hyperelastic materials is brittle in nature and can be understood using Griffith's criteria (Griffith, 1921). The fracture process in these materials involves high material and geometric nonlinearities in front of the crack tip, hence are very challenging to predict it correctly. Recently, fracture prediction using different criteria are proposed for rubber-like polymers. Averaged strain energy density criteria (ASED) by Heydari-Meybodi et al. (2019), an effective stretch criterion for mode-I crack (Ayatollahi et al., 2016) are some of the contributions.

Discrete crack modeling of fracture model the crack as displacement discontinuities. They track the crack path explicitly using additional criteria and hence computationally expensive. Phase Field Method (PFM) for modeling fracture follows a diffused crack approach. Initially used for image segmentation and micro-structure evolution, the advantages, and robustness of this method are well established (see Bourdin et al., 2000; Miehe et al., 2010) for modeling fracture. In this case, the crack propagation is easily tracked by solving the coupled governing equation in a variational setting.

Recently, attention is given to the application of PFM in modeling fracture in polymers. A rate independent micro-mechanically motivated

---

* Corresponding author.
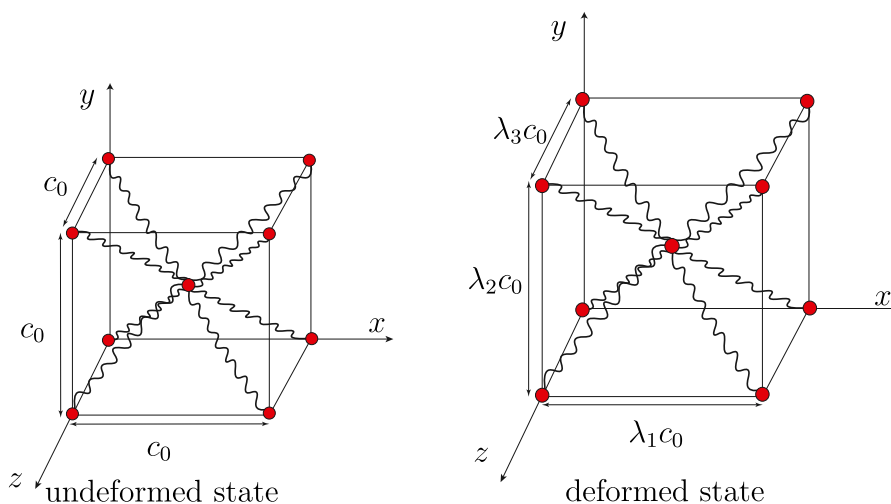 *E-mail address:* ce18resch11005@iith.ac.in (P. Aurojyoti).

Fig. 1. 8-Chain model of polymer network in a cubic representative volume element.
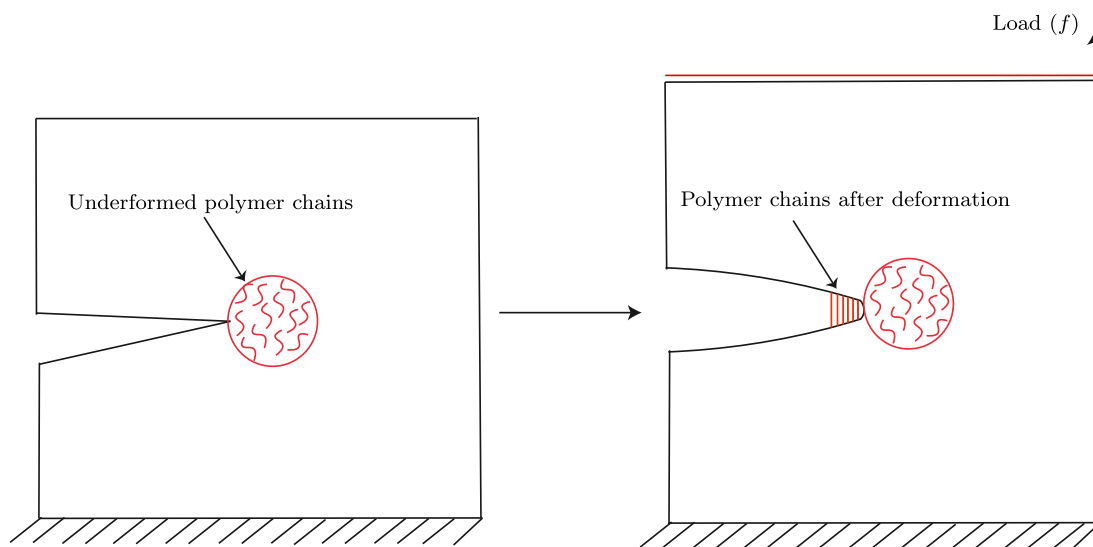

Fig. 2. (a) Polymer chains in the undeformed state (b) Stretches in the polymer chains at the crack tip due to loading.

PFM model of rubber under slow deformation process is presented in Miehe and Schänzel (2014). A comparison on strength and energy based fracture criteria is presented in an anisotropic PFM model for polymer–matrix composites by Denli et al. (2020). From numerical point of view, Peng et al. (2020) modeled the crack propagation in hyperelastic materials at large strain based on edge-based smoothed finite element method (ES-FEM). The Neo-Hooken and Mooney–Rivlin constitutive models are adopted to describe the response of rubber-like materials. At nearly incompressible limit, Ang et al. given a mixed formulation for phase field fracture in hyperelastic materials (Ang et al., 2022).

Russ et al. (2020) studied the effect of length between inclusions and size of initial notches on the fracture behavior of hyperelastic composites (soft matrix and stiff inclusions) using PFM. The breakdown mechanism of ferroelectric polymers are predicted by PFM in mechanical and electrical loading environment by Mi et al. (2021). PFM is used to predict fracture in polydisperse elastomeric networks in Li and Bouklas (2020). An inter-phase model combined with PFM for polymer composites is presented in Kumar et al. (2022). A mixed displacement-pressure formulation with phase field is proposed by Tian et al. (2022) to model fracture in nearly incompressible hyperelastic material. They addressed the issue of material intactness in the crack opening zone, when PFM is used for this type of material.

Mechanical behavior of polymers and biological tissues are dependent on strain rates. Recently, constitutive model for strain rate dependent visco-hyperelasticity is proposed (Upadhyay et al., 2020). Loew et al. (2019) included the dependency of strain rate in the constitutive description of rubber elasticity in a PFM setting. They also used an active-set strategy for incorporating damage irreversibility condition instead of using an history field $\mathcal{H}^+$, as the later still allows damage to evolve even if $\mathcal{H}^+$ is constant for a decreased strain rate. A formulation of rate effects in LS-DYNA for hyperelasticity is given by Kolling et al. (2007). A rate dependent formulation with temperature effects for rubber is studied in Trivedi and Siviour (2020).

Raina and Miehe (2015) used a rate-dependent anisotropic phase field model for predicting damage in biological tissues. Here, a stress based criteria is used for the damage driving field. Gültekin et al. (2018) proposed a rate-dependent PFM for anisotropic biological tissues which uses a energy based criteria for failure. Talamini et al. (2018) used a constitutive description for polymers that considers the effect of bond deformation and entropy in polymer chain scission process, which captures the microscopic effects. Thermo-viscoelastic analysis of polymers using PFM is studied in Arash et al. (2021). Barba et al. (2020) studied strain rate dependence on hardening and softening behavior of semi-crystalline polymers. A non-local finite deformation constitutive theory for viscoelastic material is proposed by Thamburaja et al. (2019).
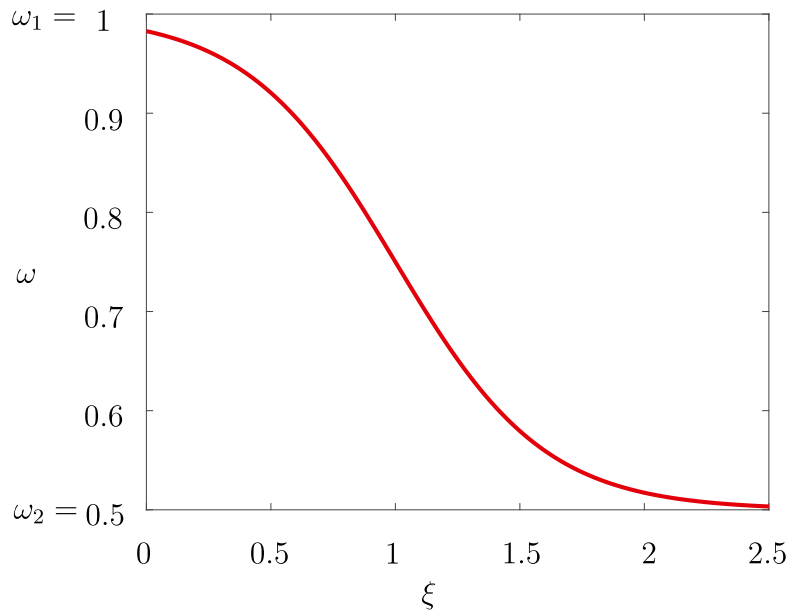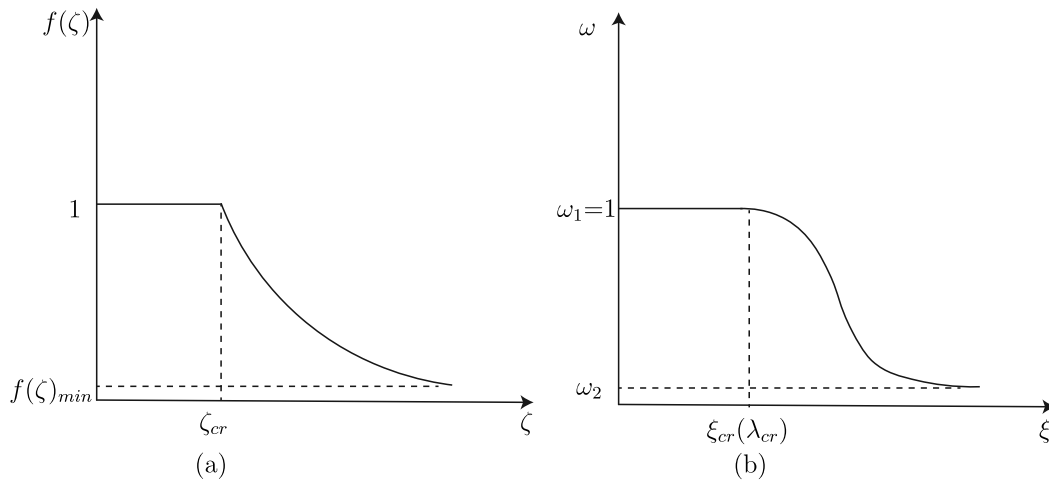
Fig. 3. Degradation pattern considered for $\mathcal{G}_c$.

Fig. 4. Degradation function adopted for $\mathcal{G}_c$ in (a) Yin and Kaliske (2020) (b) Present work, which depends on hardening parameter ζ and stretch ξ respectively.

The crack initiation is triggered by averaged Gibbs potential over the fracture process zone. In the present study, we consider only the quasi static loading condition with sufficient slow deformation rate to capture the rate-independent behavior.

Experiments on hyperelastic materials by Volokh and Trapper (2008) inferred that higher the sharpness in the crack, lower will be the fracture toughness. This is because Griffith's theory neglects the sharpness of crack tip and it is solely based on the energy balance concept. Hence, assuming a fixed value of $\mathcal{G}_c$ during crack propagation seems to largely limit the real scenario. Different energy dissipation phenomena occur at the crack tip of soft materials. In dissipative soft materials with the Mullins effect, Qi et al. (2018) proposed a method to evaluate fracture toughness. In this case, a higher amount of energy is required to propagate the crack due to bulk dissipation around the crack tip. It is observed that propagation of a crack in a particular direction is easier if certain pre-stretch is previously present perpendicular to that direction. This type of phenomena is prominent in crystallizing rubbers where stress-induced crystallization occurs in the polymeric chains (Caimmi et al., 2015). Hence, stretch at the crack tip influences the critical fracture toughness $\mathcal{G}_c$ as the material deforms. Theoretical aspect of this phenomena is less understood and mathematical modeling is

essential to predict the true behavior of these materials during crack propagation.

Failure in polymer happens mainly by two phenomena, chain scission, and cross-link failure. According to Lake and Thomas model (Lake and Thomas, 1967), the entropic part is negligible and the internal energy contributes most to the free energy during fracture. This model also emphasizes the fact that the energy required to break the chemical bond per unit cross-section is directly proportional to the elastically effective chains per unit volume (Akagi et al., 2013). Due to the effect of damage on the monomers, the elastic property of the polymer chain reduces and the number of elastically effective chains reduces per unit volume. Hence, the fracture toughness of polymer chains reduces at high stretches. At larger stretches ($\lambda \geq \lambda_L$), the fracture is controlled by internal energy contribution from the bonds of monomer, rather than contribution only from entropic part (Mao et al., 2017). Here, λ_L is the locking stretch signifying a critical value of bond stretch. This theory is applicable for polymers having strong covalent bonds, where failure happens due to chain scission rather than cross-link failure. Both of these studies motivate us to use a reduced value of critical fracture energy ($\mathcal{G}_c$), only after the critical stretch is reached or after the damage initiates. Degradation of $\mathcal{G}_c$ based on accumulated plastic
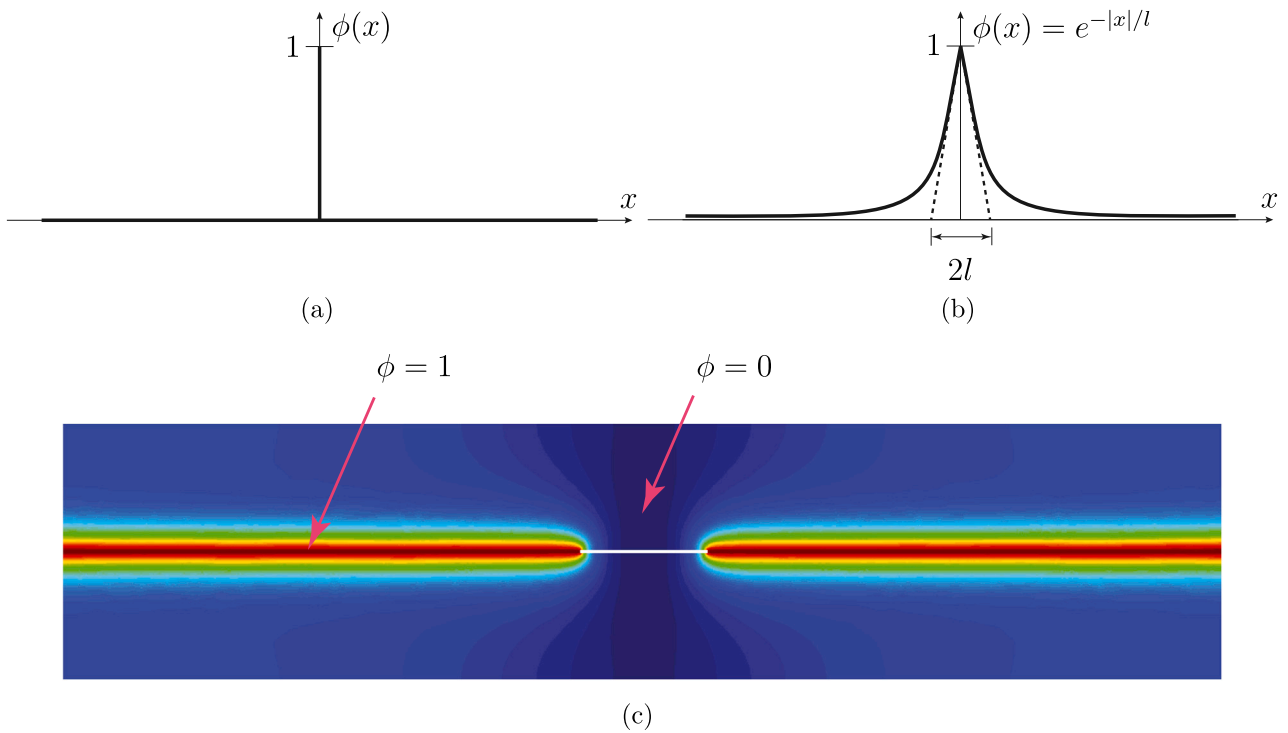
Fig. 5. Representation of (a) Discrete crack in 1D (b) Diffused crack in 1D (c) Representation of diffused crack in 2D.
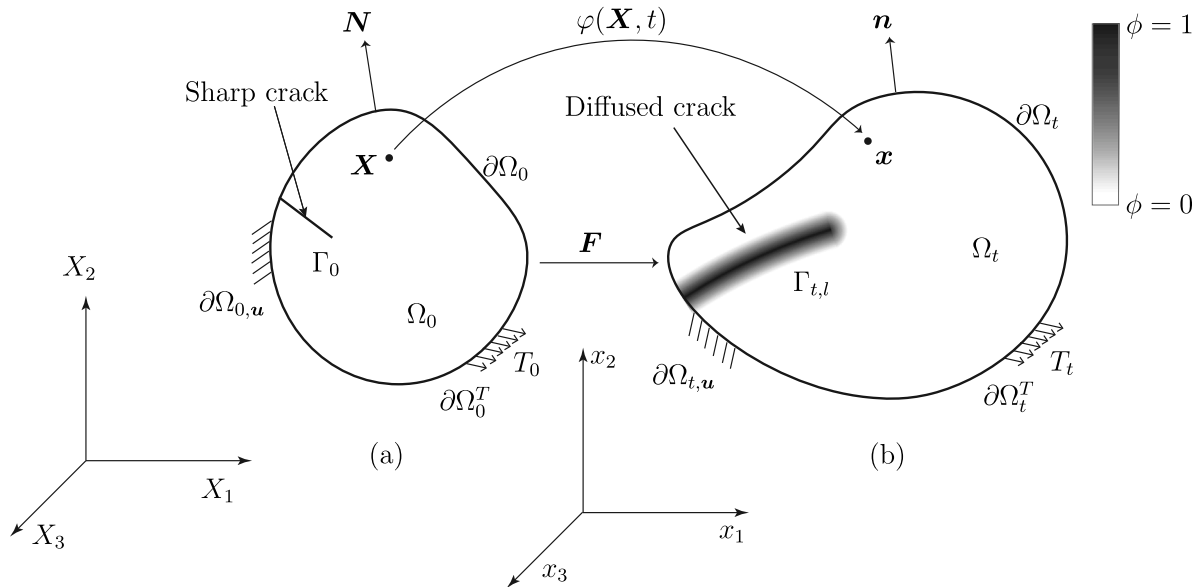

Fig. 6. (a) Reference configuration of a body with initial sharp crack Γ_0 subjected to traction force T_0 on the boundary $\partial \Omega_0^T$. Specified displacement boundary condition is given at $\partial \Omega_{0,u}$. (b) Deformed configuration of the body after a time t due to the nonlinear deformation mapping $\varphi(X)$. The regularized crack is represented in a diffused manner in the current configuration ($\Gamma_{t,l}$) with traction T_t on the boundary $\partial \Omega_t^T$.

deformation (depends on hardening) in case of ductile fracture are presented in Yin and Kaliske (2020). Modeling of fatigue crack growth using PFM in polymers, which includes the degradation of fracture toughness $\mathcal{G}_c$ by a fatigue accumulated degradation function is given in Yin et al. (2020a). Yin et al. (2020b) considered an increased value of fracture toughness for high strain rate condition during fracture, which is based on the dynamic increase factor concept. Kumar et al. (2018) treated elastomers as a phase transition solids, which facilitates to reduce the stiffness during the transition from one state to the other in a PFM setting. While the studies for reduction of $\mathcal{G}_c$ for ductile fracture above follows a quadratic variation, present study adopts an

exponential degradation of $\mathcal{G}_c$ value. In this case, degradation in the initial phase is slower and then made it to fall faster (Fig. 3). This is considered because the crack propagation becomes rapid after certain damage has been accumulated in the rubbery material. Comparison between the degradation function adopted in this work and that of literature for ductile fracture is shown in Fig. 4. Moreover, present study considers additional parameter (ρ) for the rate of degradation of $\mathcal{G}_c$ to accommodate behavior of different polymeric materials during fracture.

Energy decomposition in PFM is crucial to account for the actual energy that drives the fracture. Volumetric–deviatoric decomposition
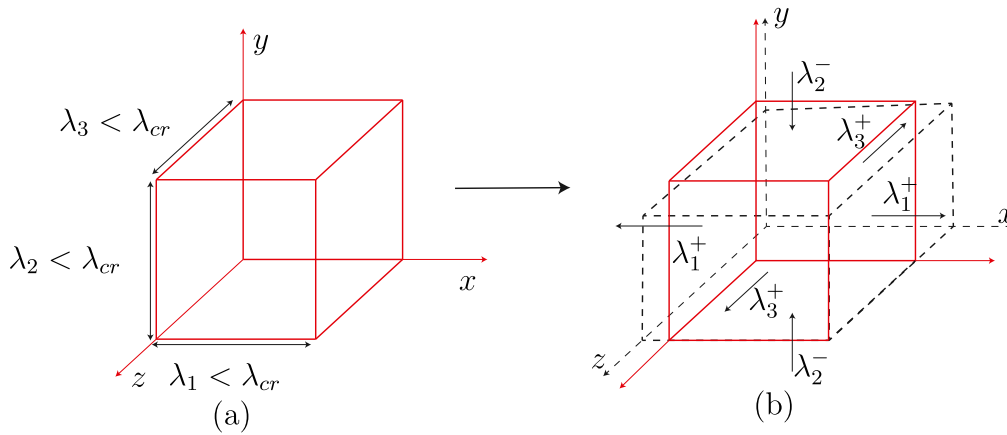
Fig. 7. (a) Stretched element for which $\Psi_0^{dev} = 0$ (b) Stretched element representing tensile and compressive stretches for which $\Psi_0^{dev} \neq 0$.
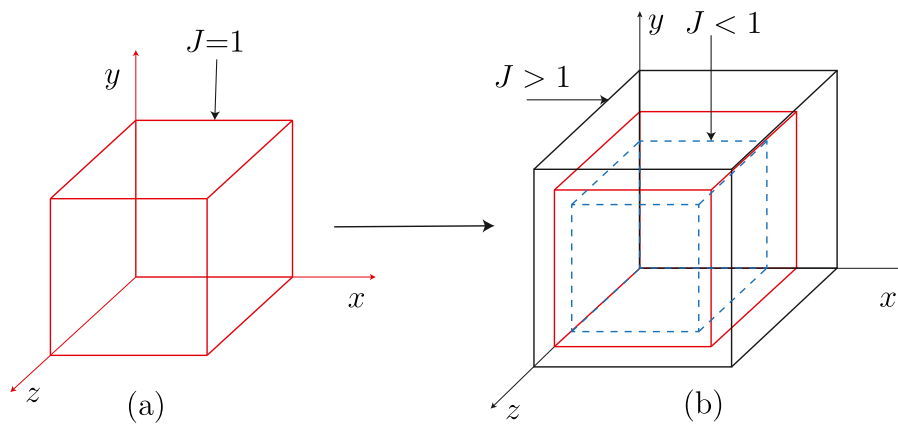

Fig. 8. (a) Element for which there is no change in volume ($\Psi_0^{vol} = 0$). (b) Element representing the volumetric change($\Psi_0^{vol} \neq 0$).
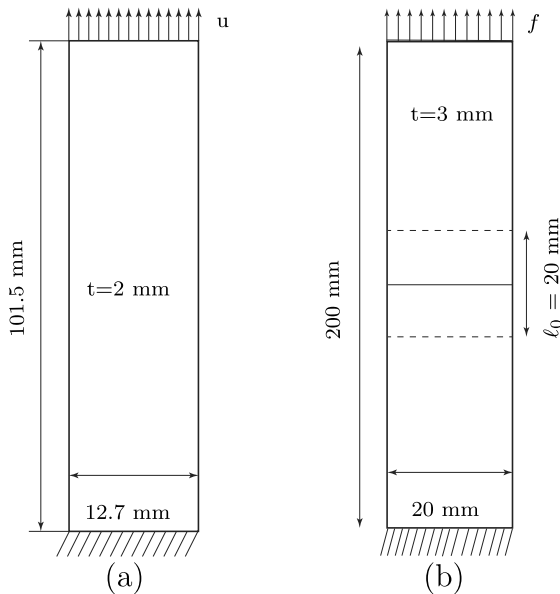

Fig. 9. (a) Uniaxial tensile test setup for SBR specimen in Pidaparti et al. (1990). (b) Uniaxial tensile test setup for SBR specimen in Hocine et al. (2002).

interpenetration in unilateral contact conditions. Tang et al. (2019) decomposed the energy based on principal stretches which are relevant in large deformation problems for the neo-Hookean type of materials. Here, the individual principal stretches contribute to either positive or negative parts of energy depending on their stretch value. In addition to the above model, Zhang et al. (2019) defined shear and bulk modulus according to tensile and compressive nature of stretch and volume change respectively for both neo-Hookean and Ogden material. Ye et al. (2020) used a Heaviside step function to eliminate the effect of Ogden parameters in evaluating active and passive parts of strain energy. Here, a displacement gradient and an enhanced deformation gradient field are used to capture the hole collapse effect in hyperelastic material. Using the principal values of strain energy density and principal directions, van Dijk et al. (2020), given a generalized strain energy decomposition for isotropic and anisotropic materials. Multiplicative decomposition of deformation gradient in terms of tensile and compressive stretches is given in Hesch and Weinberg (2014). This decomposition is only applicable for isotropic materials and in this case, polyconvexity of the strain energy functional (condition of getting at least one minimizing deformation) is not always guaranteed. For ductile type fracture at finite strains, degradation of whole deviatoric component of strain energy occurs while only volumetric tension is considered for fracture process (Ambati et al., 2016). Swamynathan et al. (2021) follows the above approach and used a Heaviside function to come up with positive and negative part of energy. This invariant-based decomposition ensures the polyconvexity of the strain energy function. Polyconvexity of strain energy agrees with the Legendre–Hadamard condition and hence it does not behave unrealistically.

The above mentioned studies split the energy into crack driving (active) and passive parts and the fracture starts instantaneously even
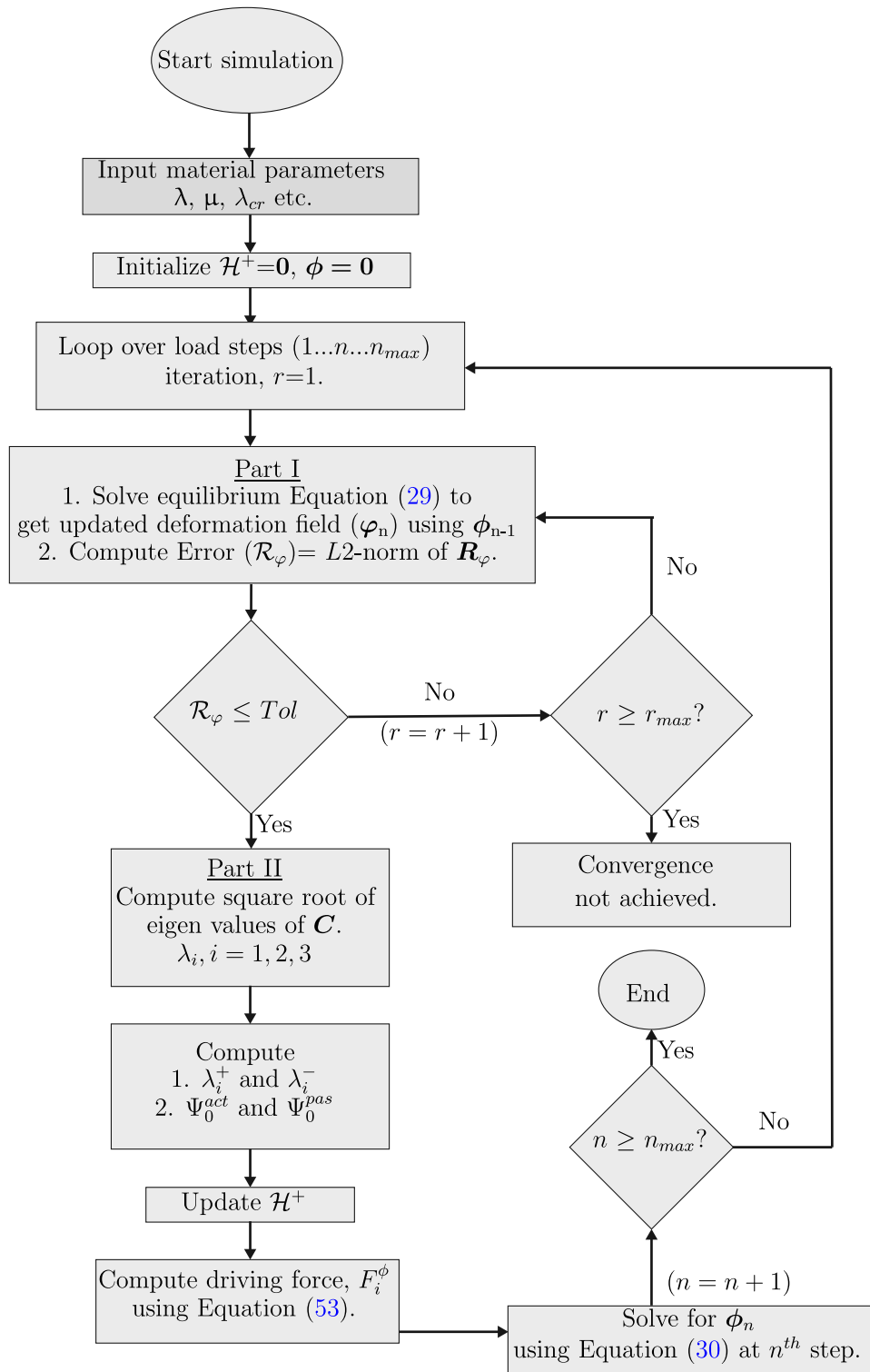
of strain energy in large deformation problems is given by Borden et al. (2016). Orthogonal decomposition of strain tensor into tensile and compressive parts is proposed by Nguyen et al. (2020) to avoid material

Fig. 10. Flow chart of the staggered solver of coupled equilibrium and phase field problem.

if the load is significantly small. In the present study, fracture driving force is zero until critical stretch is reached in the material. In this way, a critical value of stretch is used to additively decompose the strain energy into active and passive parts. Two novel extension of the phase field to model fracture in polymeric material in the present study are

- Additive decomposition of strain energy density into an active, i.e., fracture-driving part and a passive part. This is computed

based on the comparison of principal stretches to a critical value of stretch λ_{cr}.

- Degradation of critical fracture energy $\mathcal{G}_c$ beyond the critical stretch λ_{cr}, considering the dependence of $\mathcal{G}_c$ on the reduced number of elastically effective polymer chains at large stretches.

Fracture does not initiate until the critical stretch is reached and beyond which, fracture starts with a gradual reducing value of critical
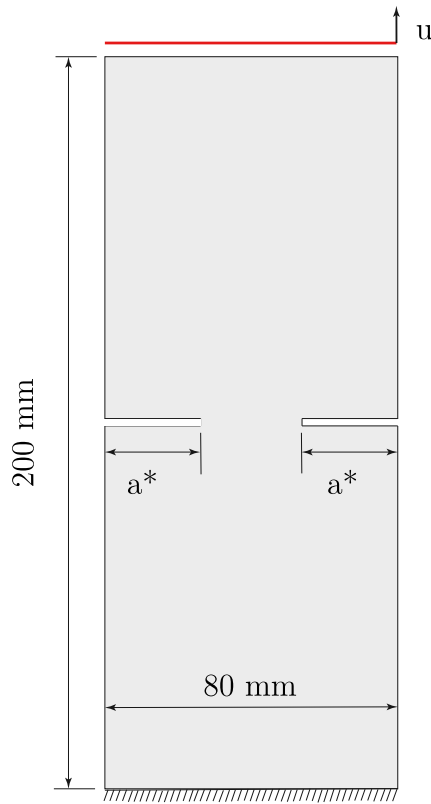
Fig. 11. DENT Specimen geometry. Bottom is fixed and uniform displacement increment is applied on the top. Initial crack length, a* = (28 mm, 20 mm and 12 mm) is taken for the analysis.

fracture toughness starting from $\mathcal{G}_c$. In this work, strain energy contributes to crack evolution only when the principal stretch is greater than the critical value. This is unlike the model presented by Tang et al. (2019) and other phase field models, where damage starts as soon as the load is applied and the fracture toughness is kept constant throughout the simulation. Total deviatoric strain energy contributes to the crack driving force as per (Ambati et al., 2016), which ignores the tensile or compressive nature of deformation. In contrary to that, present work considers only deviatoric strain energy contributed from tensile stretches ($\lambda_i > \lambda_{cr}, i = 1, 2, 3$). For the volumetric part of strain energy, crack always happens in a volumetric tension ($J \geq 1$) case and it is avoided in volumetric compression ($J < 1$). Mao et al. (2017) proposed an expression for the equivalent chain scission stretch, based on the dissociation energy of the bonds. But, the present work gives the expression for the critical stretch in terms of failure tensile stretch. The tensile stretch at the rupture is taken from the load–displacement plot provided in the literature (Hocine et al., 2002; Pidaparti et al., 1990). By using the 8-chain network model of the polymer chain, the expression for critical stretch at the continuum level in terms of multi-axial stretches is arrived. Present work and the work in Mao et al. (2017) follow the 8-chain network model to extend the chain property at the micro-level to the continuum level.

The staggered solver proposed in Miehe et al. (2010) solves the displacement field and crack phase-field separately within a Newton–Raphson iteration scheme. Within one load step, the above procedure is carried out for some minimum number of iterations to get the converged value of $\boldsymbol{u}$ and ϕ. In the present work, the displacement subproblem is solved iteratively until convergence is achieved for $\boldsymbol{u}$, and then, the crack phase field ϕ is solved in a single iteration for that particular load step. This type of solver takes relatively less computational time and is effective when the load steps are comparatively small.

1.1. Organization of the manuscript and notation used

The paper is organized as follows. The behavior of rubber-like polymer at large deformation, its network model and the proposed degradation function for critical fracture toughness $\mathcal{G}_c$ with its application is explained in Section 2. Large deformation kinematics and the concept of phase field method for fracture are described in Section 3. Total energy expression, variational form, and finite element formulation with the definition of energy decomposition are explained in Section 4. Different numerical examples are discussed to showcase the application and effectiveness of the proposed model in Section 5. Summary of the present work and some concluding remarks are presented in Section 6.

Scalars are represented as lowercase italic lightface letters like x, α. Vectors, second- and fourth-order tensors are represented by italic boldface minuscule, boldface majuscule and blackboard-bold majuscule like $\boldsymbol{x}$, $\boldsymbol{X}$ and $\mathbb{X}$ respectively. Any quantity written $\boldsymbol{X}_0$ and $\boldsymbol{X}_t$ indicates that $\boldsymbol{X}$ is defined in reference and current configuration respectively. The (ij) component of a second order tensor $\boldsymbol{A}$ is represented by A_{ij} and $\mathbb{A}_{ijkl}$ represents the $(ijkl)$ component of a fourth order tensor $\mathbb{A}$.

2. Physics of rubber-like polymer at large strain

Rubber-like polymers consist of flexible long chains with random orientations. Each molecular bond allows to change the direction of the sub-units because of the rotational freedom. Thus, the molecular chains can tangle with adjacent chains and form cross-links among themselves. Bond stretching and chain straightening occur in the direction of the applied load. These phenomena are responsible for the elastic behavior of rubbery polymers. Before the chain stretches, unfolding of the chain happens from the original state due to the application of external load.

The behavior of rubber at a macroscopic scale can be known from individual polymeric chains by considering models in which groups of chains are arranged in a certain manner. Therefore, the constitutive model relating to the deformability of a single chain of polymer is more appealing. Accordingly, various models such as 3-chain model, 4-chain model, 8-chain model (Arruda and Boyce, 1993), full network model (Wu and Van Der Giessen, 1993) are proposed. These models are based on the statistical mechanics approach of rubber elasticity. Among these, the 8-chain model predicts the experimental observations with high accuracy (Boyce and Arruda, 2000).

Considering the effect of surrounding chains and links, non-affine deformation occurs in a chain i.e., the actual deformation in the chain is less than the expected stretch. If 'ℓ' is the length of each sub-unit and 'n' is the number of sub-units in an unstrained chain, then from a statistical point of view, the root mean square length of the chain is $\sqrt{n}\ell$. Hence in a cubic representation of 8 similar chains (Fig. 1), the relationship between chain stretch (λ_{ch}) and multiaxial stretches ($\lambda_1, \lambda_2, \lambda_3$) is obtained from Boyce and Arruda (2000) as

$$\lambda_{ch} = \sqrt{\frac{\lambda_1^2 + \lambda_2^2 + \lambda_3^2}{3}} . \tag{1}$$

This hypothesis is assumed to reflect the behavior of all chains and links that constitute the network. At a very large deformation, the chains tend to align in the direction of applied load and get stretched considerably until failure happens.

2.1. Critical stretch

During the application of load, polymer chains undergo straightening and stretching. As a result, the state of stress near the crack tip is almost same as in case of uniaxial tension for both mode-I (Long et al., 2011; Gao, 1997) and mixed mode (I/II) fracture (Zhou and Gao, 1998; Hamdi et al., 2007). This assumption is valid only when the material undergoes a considerable amount of stretch before fracture and it is used to get the critical value of the chain stretch (λ_{cr}). Let $\lambda_{tensile}$ be
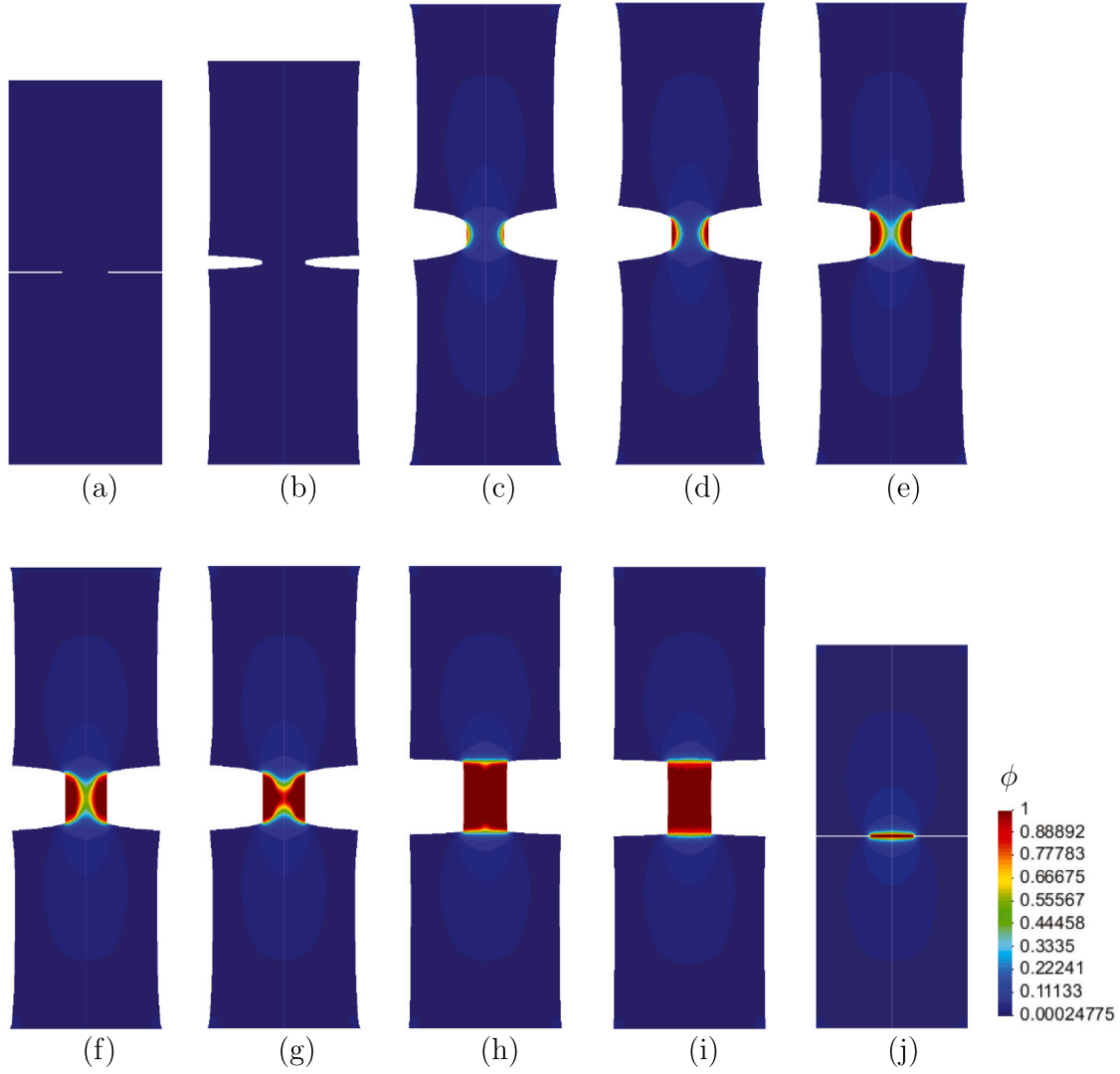
Fig. 12. Crack pattern at the displacement of (a) $u = 0$ or undeformed state, (b) $u = 10$ mm, (c) $u = 40.15$ mm, (d) $u = 40.35$ mm, (e) $u = 40.49$ mm, (f) $u = 40.51$ mm, (g) $u = 40.53$ mm, (h) $u = 40.54$ mm, (i) $u = 40.55$ mm. (j) Crack pattern in reference configuration in the DENT specimen with initial crack length of 28 mm and length scale $l = 1$ mm.

the stretch measured at the final rupture in the uniaxial tensile test of a standard specimen. We have $\lambda_1 = \lambda_{tensile}$ in one direction at the onset of fracture. Assuming nearly incompressible behavior of rubbery polymer ($J = \lambda_1 \lambda_2 \lambda_3 \approx 1$), we have

$$\lambda_2 = \lambda_3 = \frac{1}{\sqrt{\lambda_1}} = \frac{1}{\sqrt{\lambda_{tensile}}} \quad , \tag{2}$$

and we get the critical stretch of the chain from Eq. (1) as

$$\lambda_{cr} = \sqrt{\frac{\lambda_{tensile}^3 + 2}{3\lambda_{tensile}}} \quad . \tag{3}$$

2.2. Reduction of fracture toughness based on stretches

Considering the degradation of the elastic property of the polymer chains as a result of damage, reduction in fracture toughness is considered based on the stretch value at any material point. Considering only for rate-independent case (without any bulk dissipation phenomena in front of the crack tip), we define a simple expression for gradually reducing fracture toughness ($\mathcal{G}_{rd}$) as a function of stretch in the loading direction (λ). This is applicable when the condition of $\lambda \geq \lambda_{cr}$ is satisfied. We have adopted Eq. (4) to incorporate the degradation of

fracture toughness value according to the stretch. A schematic diagram for the stretch of polymer chains in front of the crack is given in Fig. 2. Here, we do not consider the effect of strain-induced crystallization, due to which there is a relative increase in the value of $\mathcal{G}_c$ because of the alignment of polymers in the direction of the applied load. This phenomena happens at a relatively higher temperature well above the crystallization temperature and it is out of the scope of this study.

Reduced value of $\mathcal{G}_c$ is expressed as

$$\mathcal{G}_{rd} = \omega \mathcal{G}_c \quad . \tag{4}$$

Here, ω is a reducing factor for $\mathcal{G}_c$ which is expressed as

$$\omega = \left[\omega_1 + (\omega_2 - \omega_1)(1 - D) \right], \quad D(\xi) = \frac{1}{1 + e^{\frac{-(1-\xi)}{\rho}}} \quad , \tag{5}$$

ξ is given in terms of stretch.

$$\xi = \lambda_{cr} + \left(\frac{\lambda}{\lambda_{cr}} - 1 \right) \quad . \tag{6}$$

The reducing factor satisfies the properties $0 < \omega \leq 1$, $\omega(\xi < \xi_{cr}) = 1$. with maximum value of $\omega_1 = 1$ and minimum value of ω_2 as per the percentage of degradation.

Here, $\rho (= 0.2)$ is a parameter which controls the rate of transition between ω_1 and ω_2 with respect to ξ. By choosing $\omega_1 = 1$ and $\omega_2 =$
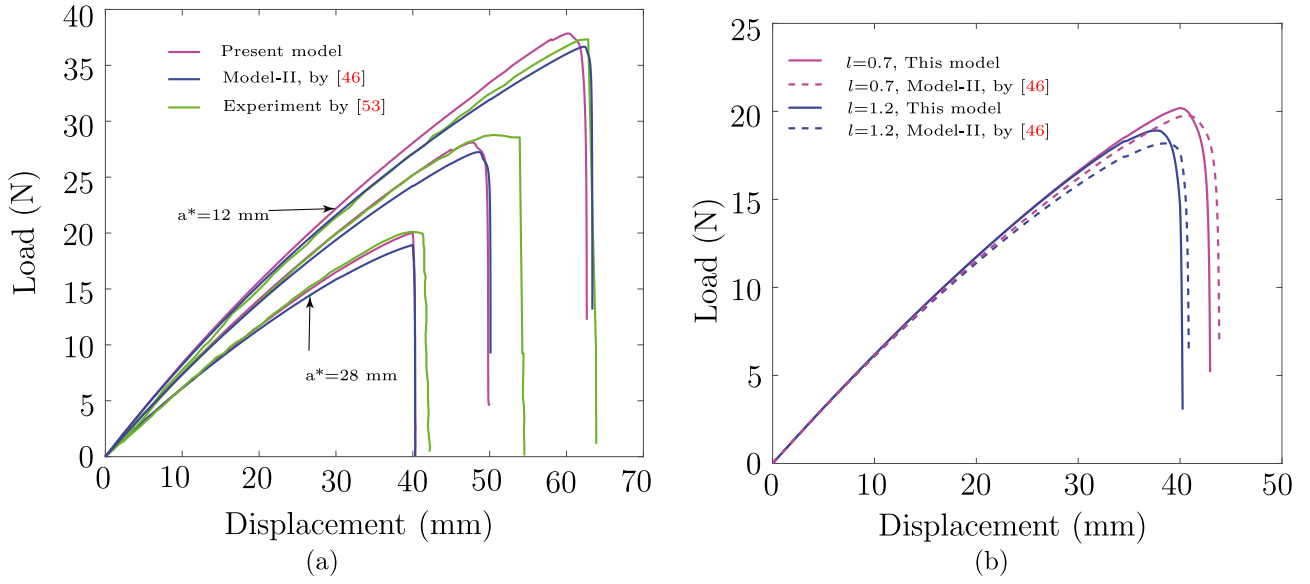
Fig. 13. (a) Comparison of load displacement plot for DENT specimen with initial edge crack length a* = 28 mm, 20 mm and 12 mm for a length scale l = 1 mm (b) Comparison of load displacement plot for different length scale using critical stretch of 1.61 and without using stretch criteria.

0.5, we can vary the value of ω between 1 and 0.5 for a range of ξ values (Fig. 3). From the nature of function, it is verified that $\mathcal{G}_c$ is reduced to almost a constant value after certain value of stretch. Eq. (5) is multiplied by a factor of 1.1 to get a lesser reduction effect. By considering ω_2 value to be 0.5, 0.6 and 0.7, we achieve a 7, 12 and 18 percent reduction in $\mathcal{G}_c$ respectively (Fig. 16). λ is the stretch at any material point in the loading direction and λ_{cr} is the critical stretch. Eq. (4) is used only if the condition $\lambda \geq \lambda_{cr}$ is satisfied.

Critical fracture toughness ($\mathcal{G}_c$) of rubber-like polymer is adopted from Miehe and Schänzel (2014) considering the dissociation energy of monomers in a polymer molecules. The extent of degradation can be controlled by ω_2 and ρ. These values can be dependent on different loading conditions and the material under consideration. More reduction should be considered for relatively sharp notch, like in case of glassy polymers and less reduction can be considered for materials those have relatively larger blunt notch during crack propagation.

3. Phase field method for hyperelastic material

In this section, the formulation of the phase-field fracture model in the context of large deformation problems is presented. Decomposition of strain energy density is proposed based on the critical stretch value of the material.

3.1. Crack topology and regularized fracture energy

PFM approximates a sharp crack as a smeared crack by introducing a length scale. The order parameter ($\phi := \phi(X, t)$) that represents the extent of fracture varies exponentially (Eq. (8)) between $\phi = 0$ (unbroken state) and $\phi = 1$ (fully broken or separated state), see Fig. 5(c). Topology of discrete and smeared crack is shown in Fig. 5(a) and Fig. 5(b) respectively. The representation of crack in a discrete sense is represented as

$$\phi(x) = \begin{cases} 1 & \text{if } x = 0. \\ 0 & \text{otherwise.} \end{cases} \tag{7}$$

and in smeared sense, it is represented as

$$\phi(x) = e^{-|x|/l}, \quad -\infty \leq x \leq +\infty . \tag{8}$$

Above equation satisfies the condition for ϕ as

$$\phi(0) = 1 \quad \text{and} \quad \phi(\pm\infty) = 0 \tag{9}$$

In the context of large deformation, let us consider a deformable body in the reference configuration $\Omega_0 \subset \mathcal{R}^n$, $n \in [2, 3]$ enclosed by the surface $\partial\Omega_0$ (Fig. 6(a)) having normal to the surface N has undergone a nonlinear deformation by a function $\varphi(X, t)$ to reach a current position $\Omega_t \subset \mathcal{R}^n$ after time $t \subset \mathcal{T}$. The position vector of material points in Ω_0 are given by X which moves to x in the current configuration (Fig. 6(b)). The body is subjected to traction, T on the boundary. The deformation field is defined as

$$\varphi : \begin{cases} \Omega_0 \times \mathcal{T} \to \mathcal{R}^n, n \in [2, 3] \\ (X, t) \longmapsto \varphi(X, t). \end{cases} \tag{10}$$

Then deformation gradient F is defined as

$$F = \nabla_X \varphi = \frac{\partial x}{\partial X} . \tag{11}$$

The determinant of F is denoted by $J = \frac{dv}{dV} > 0$ which determines the amount of volume change, where dv and dV are the infinitesimal volume elements in current and reference configuration respectively. As the body evolves through time $\mathcal{T} \subset \mathcal{R}$, the space- and time-dependent crack phase field ϕ is defined as

$$\phi : \begin{cases} \Omega_0 \times \mathcal{T} \to [0, 1]. \\ (X, t) \longmapsto \phi(X, t). \end{cases} \tag{12}$$

It is readily observed that Eq. (8) is the solution to the homogeneous differential equation of the form below.

$$\phi(x) - l^2 \frac{d^2\phi(x)}{dx^2} = 0. \tag{13}$$
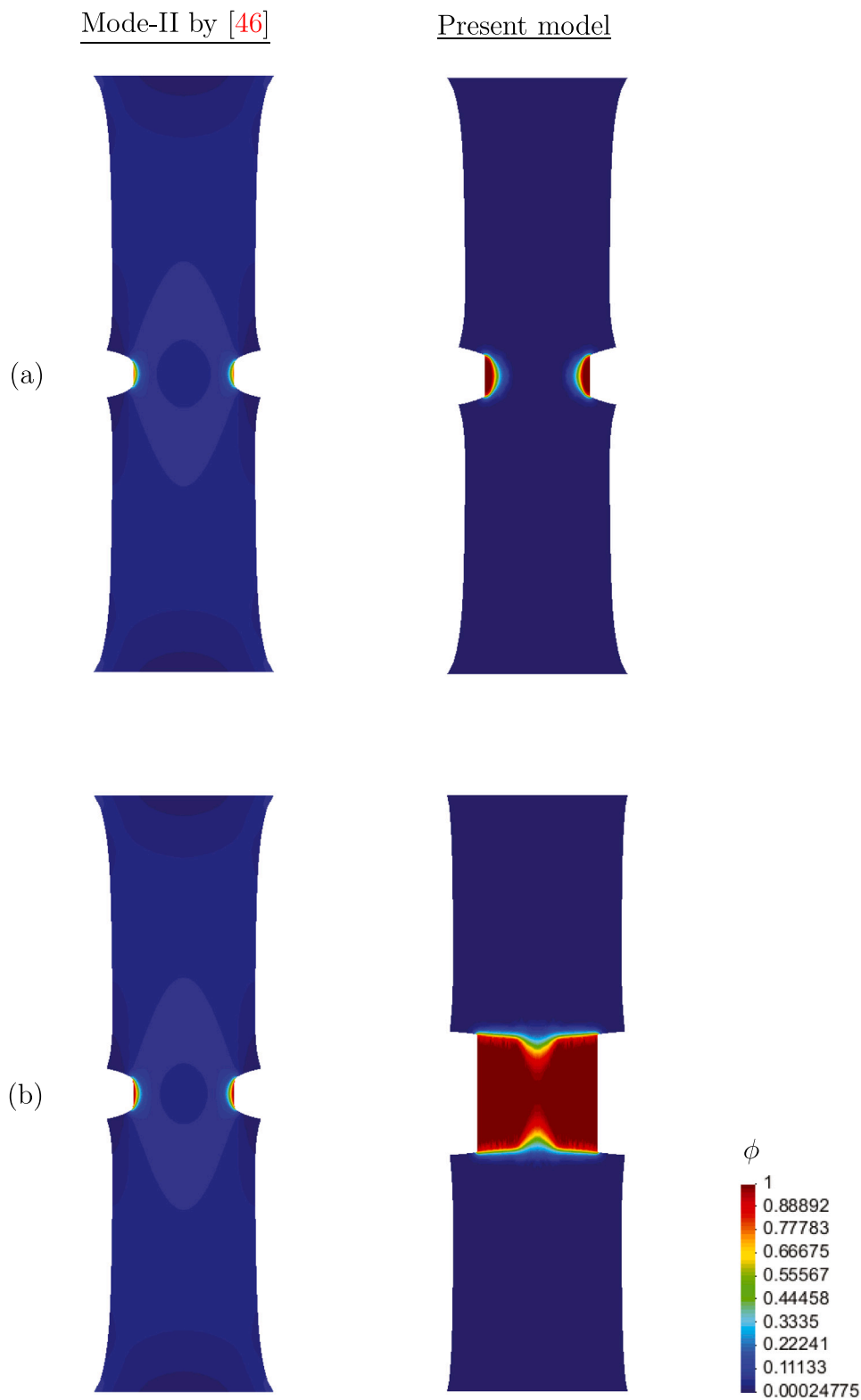
with constraints in Eq. (9).

Fig. 14. Comparison of crack pattern in DENT specimen with initial crack length of a* = 12 mm and length scale l = 1 mm, at a displacement of (a)62.37 mm (b) 62.75 mm.

Euler equation of the following variational principle gives the differential equation of the form (13).

$$\phi = Arg[\underset{\phi \in \zeta}{Inf} \ H(\phi)] \tag{14}$$

where $\zeta = \{\phi | \phi(0) = 1, \ \phi(\pm\infty) = 0\}$, with the functional $H(\phi)$ of the form,

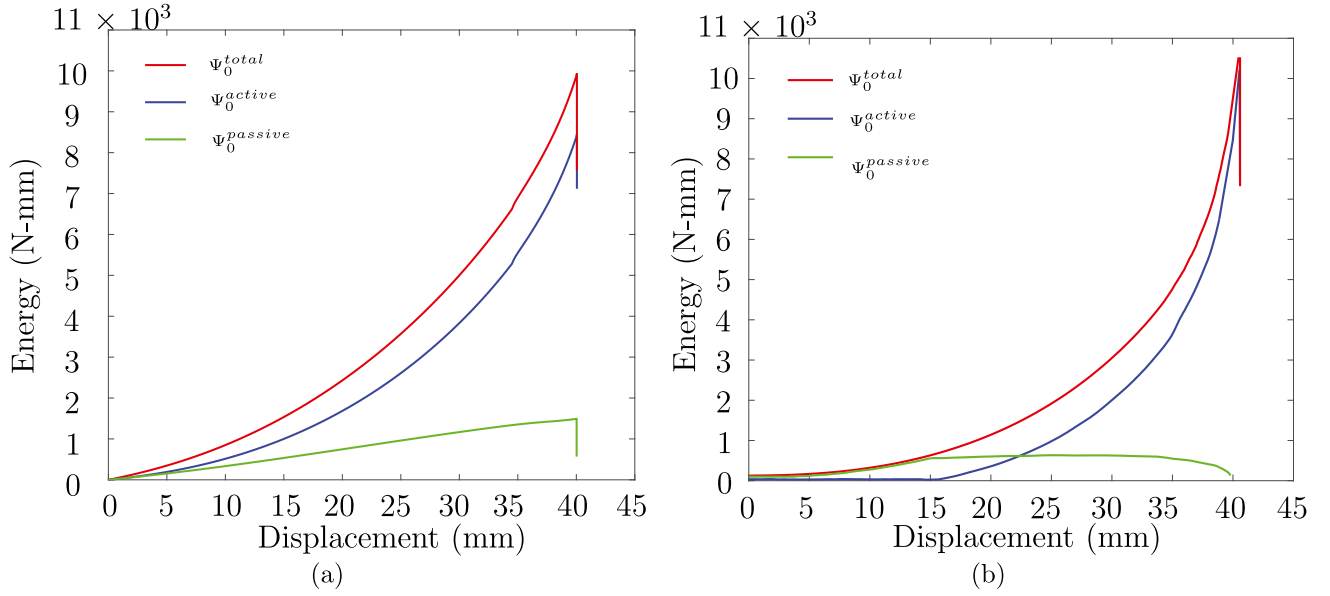$$H(\phi) = \frac{1}{2} \int_{\Omega_0} (\phi^2 + l^2 \phi'^2) d\Omega_0. \tag{15}$$

Fig. 15. Plot of active energy, passive energy and total energy as the load is applied to the DENT specimen ($a^* = 28$ mm) for length scale $l = 1$ mm (a) Without using stretch criteria (b) Using stretch criteria (Present model).
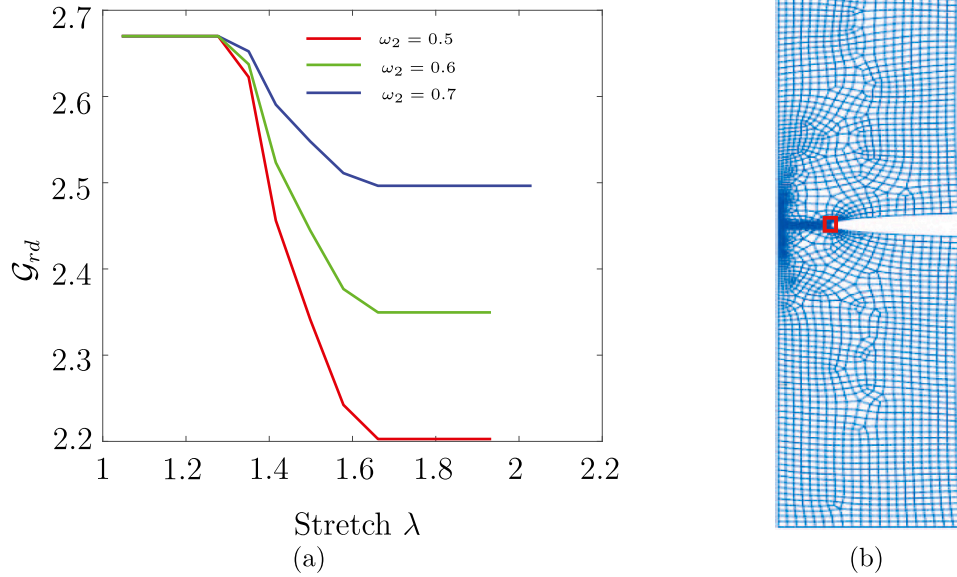

Fig. 16. (a) Reduction of $\mathcal{G}_c$ value from 2.67 with stretch for various values of ω_2. (b) 0.3 mm square region selected for calculation of average $\mathcal{G}_{rd}$ and average stretch λ in Figure (a) for DENT ($a^* = 28$ mm) specimen.

We get $H(\phi) = l\Gamma_0$, if we use $d\Omega_0 = \Gamma_0 dx$ in Eq. (15) at $\phi = e^{\frac{-|x|}{l}}$.

$$\implies \Gamma_{0,l} = \frac{1}{l}H(\phi) = \int_{\Omega_0}\left(\frac{\phi^2}{2l} + \frac{l}{2}|\nabla\phi|^2\right)d\Omega_0 = \int_{\Omega_0}\gamma_l(\phi,\nabla\phi)d\Omega_0.$$

(16)

In a limiting sense, as $l \to 0$, the regularized crack surface becomes a discrete crack surface (Bourdin et al., 2000).

$$\lim_{l\to 0}\Gamma_{0,l} = \lim_{l\to 0}\frac{H(\phi)}{l} \approx \Gamma_0.$$

(17)

The regularized fracture energy in the system for the evolved crack surface, which is defined in terms of critical fracture energy along with

crack density functional is written as

$$E_0^{frac} = \mathcal{G}_c\int_{\Gamma_0}d\Gamma_0 = \int_{\Omega_0}\gamma_l(\phi,\nabla\phi)\mathcal{G}_c\,d\Omega_0, \quad \gamma_l = \frac{\phi^2}{2l} + \frac{l}{2}|\nabla\phi|^2.$$

(18)

Where $\mathcal{G}_c$ is the critical fracture energy of the material. From the mesh discretization point of view, the condition of ($h \leq \frac{l}{2}$) needs to be met for resolving the length scale. In other words, a minimum of 4 elements has to be inside the diffusive crack band to get the value of regularized crack surface energy $\Gamma_{0,l}$ close to sharp crack Γ_0. Expression for critical stress for 1D-bar, which depends on the critical fracture energy ($\mathcal{G}_c$) and the length scale (l) is given by $\sigma_c = \frac{9}{16}\sqrt{\frac{E\mathcal{G}_c}{3l}}$ (Borden et al., 2012). The symbols carry their usual meaning. Hence, the length scale (l)
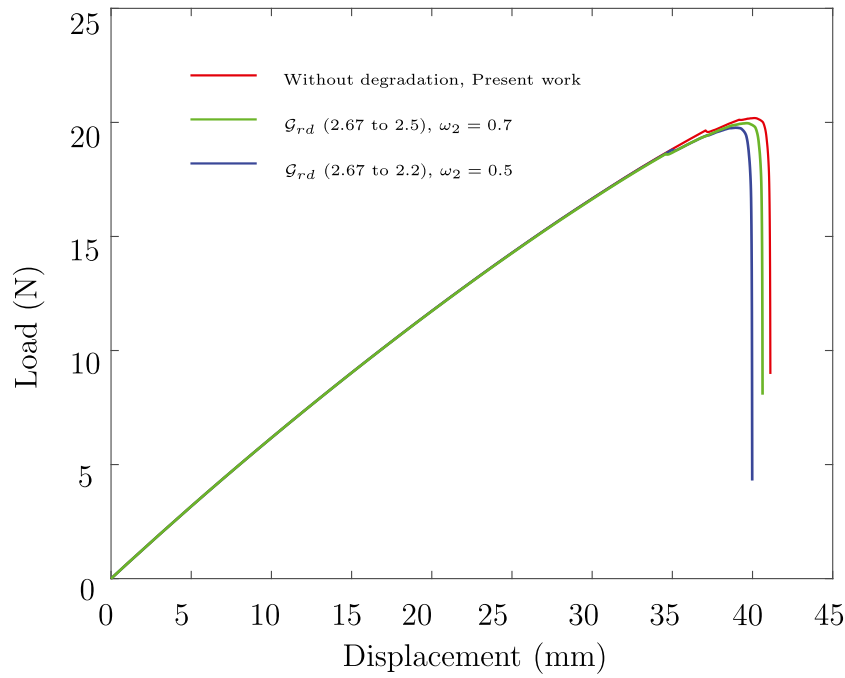
Fig. 17. Load vs displacement response for without degradation and various reduced values of $\mathcal{G}_c$ according to stretch in front of crack (DENT specimen- a* = 28 mm, l = 1 mm).
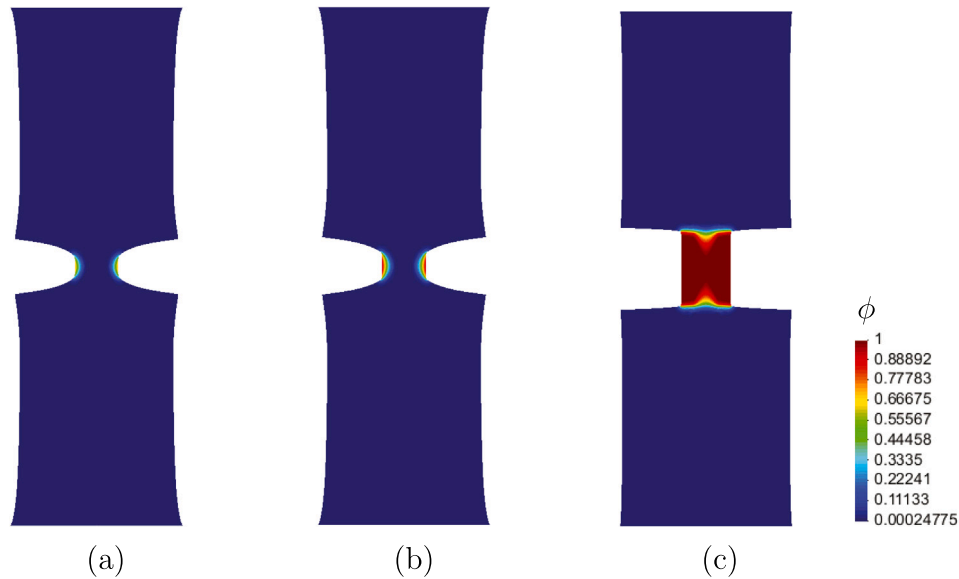

Fig. 18. Crack pattern obtained at the displacement of 40 mm with initial crack length of 28 mm and length scale l = 1 mm.(a) Present model without degradation of $\mathcal{G}_c$ (b) with degradation of $\mathcal{G}_c$ from 2.67 N/mm to 2.5 N/mm (c) with degradation of $\mathcal{G}_c$ from 2.67 N/mm to 2.2 N/mm.

is certainly associated with the material under consideration and it needs to be calibrated through experiments. The chosen value of the length scale affects the load–deflection behavior as it affects the value of critical stress. Therefore the length scale (l) chosen affects the peak load and the displacement at which the fracture starts.

3.2. Dissipation function and crack irreversibility condition

Once the crack has formed it cannot be healed. To prevent the healing of the crack, a crack irreversibility condition is used. The evolution of regularized crack with time has to satisfy the following equation for the crack to be irreversible. Let us assume E_0^{int} is the total internal energy potential of the system. The total dissipation for the

rate-dependent case is written as

$$-\frac{\delta E_0^{int}}{\delta \phi} \dot{\phi} = k\langle \dot{\phi} \rangle + \alpha \langle \dot{\phi} \rangle^2 \geq 0. \tag{19}$$

Here, α is a numerical constant, known as the viscous regularization parameter used for rate-dependent case. To satisfy the above condition of Eq. (19),

$$\dot{\phi} = 0, \quad \text{if} \quad -\frac{\delta E_0^{int}}{\delta \phi} < k \quad \text{(or)} \quad \alpha \dot{\phi} = \langle -\frac{\delta E_0^{int}}{\delta \phi} - k \rangle \tag{20}$$

Where

$$-\frac{\delta E_0^{int}}{\delta \phi} = \left[g'(\phi) \Psi_0 + \frac{\partial(\gamma_l \mathcal{G}_c)}{\partial \phi} - \nabla \cdot \frac{\partial(\gamma_l \mathcal{G}_c)}{\partial \nabla \phi} \right]. \tag{21}$$
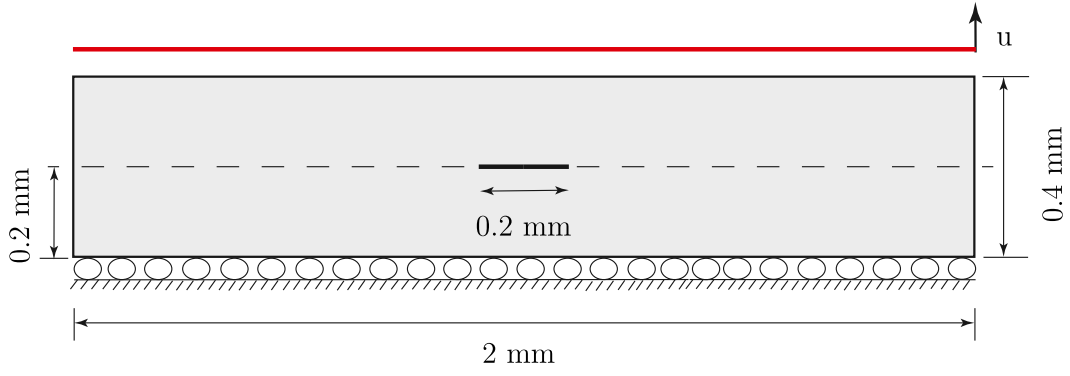
Fig. 19. Penny shaped precracked specimen geometry. The notch width is symmetrically placed at the center and its width is 0.005 mm. Bottom of the specimen is restrained against *y*-direction and one node at the middle is restrained against *x*-direction. Uniform displacement increment is applied on the top.
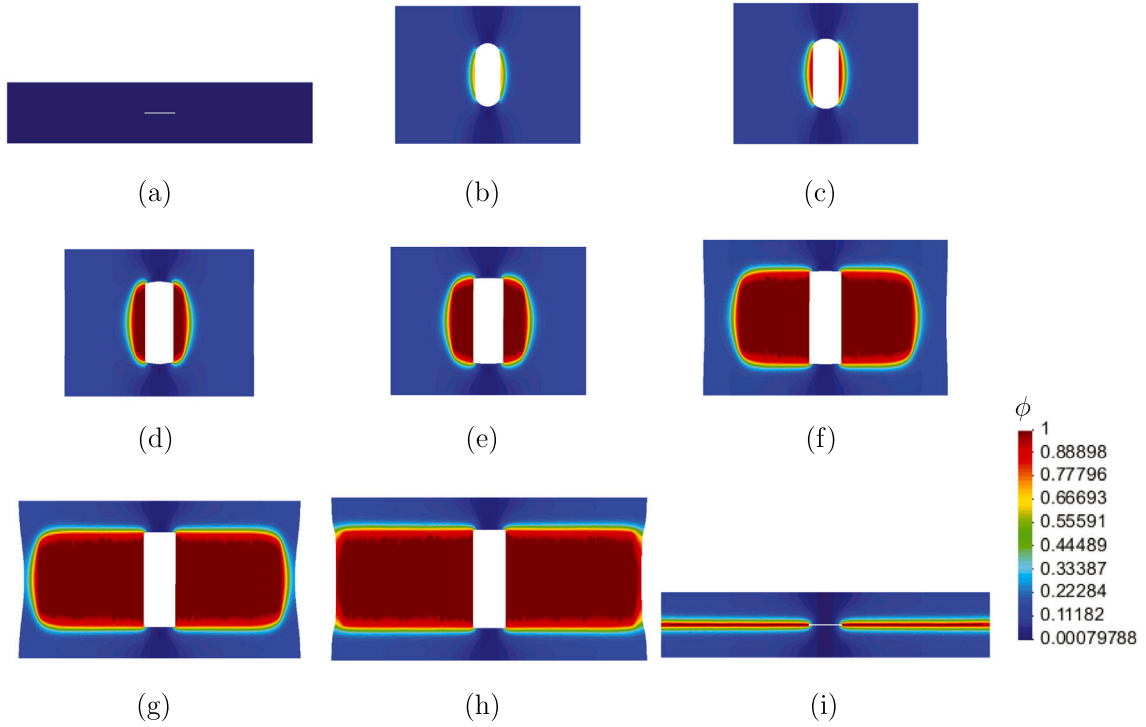

Fig. 20. Crack pattern at the displacement of (a) Initial configuration or $u = 0$ (b) $u = 0.456$ mm (c) $u = 0.476$ mm (d) $u = 0.516$ mm (e) $u = 0.536$ mm (f) $u = 0.576$ mm (g) $u = 0.592$ mm (h) $u = 0.5952$ mm applied for length scale $l = 0.02$ mm in penny shaped precracked specimen. Smallest element size of 0.0025 is considered in the expected crack region. (i) Crack pattern in the reference configuration.

Here, $\dot{\phi}$ evolves according to the viscous over-force $\left(-\frac{\delta E_0^{int}}{\delta \phi} - k \right)$. k is the threshold. The term $g'(\phi)\Psi_0$ is the energetic force defined as

$$g'(\phi)\Psi_0 = -2(1-\beta)(1-\phi)\Psi_0. \tag{22}$$

Note that the total resistance is offered by crack phase field ($\mathcal{G}_c \delta_\phi \gamma_l$) and the viscous term ($\alpha\dot{\phi}$) defined in Eq. (20). This is against the local driving force, known as history field $\mathcal{H} = \underset{t\in[0,\mathcal{T}]}{\text{Max}}(\Psi_0)$. This formulation is thermodynamically consistent because the positive dissipation condition is always satisfied by Eq. (19). As the value of α approaches zero, we get the rate-independent response of the system. The artificial viscous parameter (α) tends to dissipate more energy during the evolution of fracture. This regularized viscous formulation is followed in this work which is essential to prevent numerical instability and convergence issues of the FE solver for large deformation cases. Value of (α) is set as 0.001 $\frac{\text{N·s}}{\text{mm}^2}$ for all simulations unless mentioned otherwise. We can have the formulation without α term but in that case, the load drop suddenly occurs as the fracture starts in the material. Also,

numerical instability and mesh distortion occur [$\det(\mathbf{F}) < 0$] in case of large deformation problems. Whereas, for small deformation problems, the formulation works well without any numerical instability.

4. Formulation

The total energy of the system is contributed by elastic strain energy, fracture energy, and external energy which is represented as a functional given below.

$$E_{total}(\boldsymbol{\varphi}, \phi) = E_0^{int} + E_0^{ext}. \tag{23}$$

The internal energy of the system consists of the strain energy stored in the body due to deformation and the energy due to fracture.

$$E_0^{int}(\boldsymbol{\varphi}, \phi) = \int_{\Omega_0} g(\phi)\Psi_0 d\Omega_0 + \int_{\Omega_0} [\gamma_l(\phi, \nabla\phi)\mathcal{G}_c + \alpha\dot{\phi}]d\Omega_0. \tag{24}$$
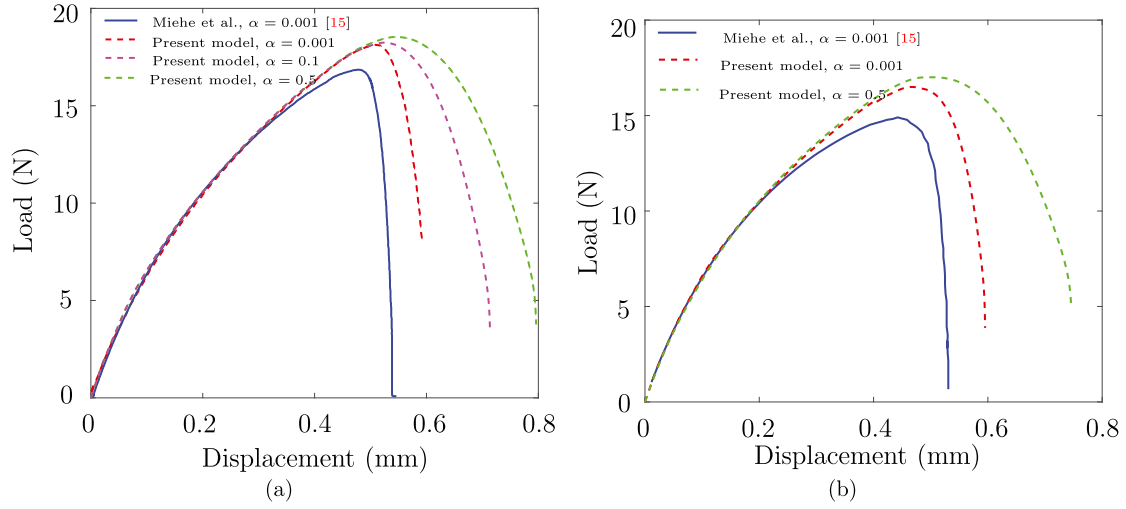
Fig. 21. Comparison of load displacement plot for penny shaped precracked specimen with (a) length scale $l = 0.01$ mm (b) length scale $l = 0.02$ mm.
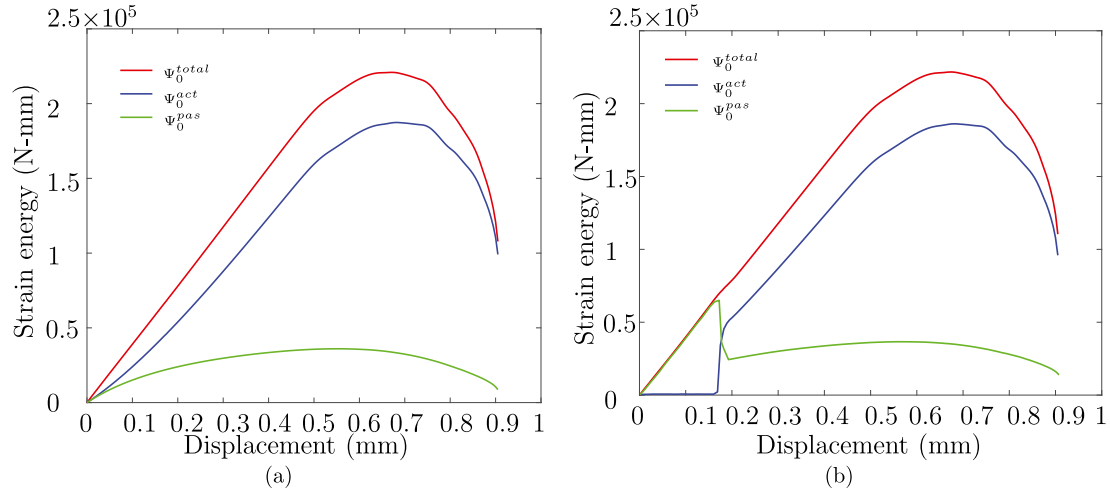

Fig. 22. Plot of active energy, passive energy and total energy as the load is applied to the penny shaped precracked specimen for length scale $l = 0.02$ mm and $\alpha = 0.5$ N-s/mm^2 (a) Without using stretch criteria (b) Using stretch criteria (Present model).

The external energy contributed from traction in the boundary and body forces is defined as,

$$E_0^{ext} = -\int_{\Omega_0} \boldsymbol{B} \cdot \boldsymbol{\varphi} \, d\Omega_0 - \int_{\partial\Omega_0^T} \boldsymbol{\varphi} \cdot \boldsymbol{T} \, dA \ . \tag{25}$$

The elastic stiffness is degraded by the function $g(\phi)$, as some part of the elastic strain energy is used for the crack formation. This degradation function facilitates the coupling of the equilibrium equation with the phase field sub-problem. A quadratic degradation function of the form $g(\phi) = (1-\beta)(1-\phi)^2 + \beta$ is considered which follows the constraints $g(0) = 1$, $g(1) = 0$, $g'(1) = 0$. β is a very small numerical constant used to prevent the ill-conditioning of stiffness matrix when the phase field $\phi = 1$ or when the material is completely damaged. If β is not included in the degradation function, $[g(\phi) = (1-\phi)^2]$ becomes zero when $\phi = 1$. This makes the tangent operator vanish and it destabilizes the solver. $\beta = 10^{-8}$ is taken for all simulations in this study. It makes the stress values to be almost near zero, if not equal to zero when $\phi = 1$. Hence this value should be kept small enough not to have any significant stress values when $\phi = 1$.

4.1. Variational form

The first variation of the internal strain energy (E_0^{int}) is written as

$$\delta E_0^{int}(\boldsymbol{\varphi}, \delta\boldsymbol{\varphi}, \phi, \delta\phi) = -\int_{\Omega_0} \delta\boldsymbol{\varphi} \operatorname{Div} \boldsymbol{P} \, d\Omega_0 - \int_{\Omega_0} 2(1-\beta)(1-\phi)\Psi_0\delta\phi \, d\Omega_0,$$

$$+ \int_{\Omega_0} \left[\frac{\mathcal{G}_c}{l}\phi\delta\phi - \mathcal{G}_c l \nabla_X \phi \cdot \nabla_X(\delta\phi) + \alpha\delta\phi \right] d\Omega_0 + \int_{\partial\Omega_0} \delta\boldsymbol{\varphi} \, \boldsymbol{P} \cdot \boldsymbol{N} \, dA$$

$$+ \int_{\partial\Omega_0} \delta\phi \mathcal{G}_c l \nabla_X \phi \cdot \boldsymbol{N} \, dA = 0 \ . \tag{26}$$

where, the degraded first Piola–Kirchhoff stress is defined as

$$\boldsymbol{P}(\boldsymbol{F}, \phi) = g(\phi)\frac{\partial\Psi_0}{\partial\boldsymbol{F}} \ . \tag{27}$$

First variation of the external energy is

$$\delta E_0^{ext}(\boldsymbol{\varphi}, \delta\boldsymbol{\varphi}) = -\int_{\Omega_0} \delta\boldsymbol{\varphi} \cdot \boldsymbol{B} \, d\Omega_0 - \int_{\partial\Omega_0^T} \delta\boldsymbol{\varphi} \cdot \boldsymbol{T} \, dA = \boldsymbol{F}_{\boldsymbol{\varphi}}^{ext}. \tag{28}$$

Equating the individual variations to zero, the governing equations are obtained as

$$\operatorname{Div} \boldsymbol{P} + \boldsymbol{B} = 0 \quad \text{in} \quad \Omega_0, \tag{29}$$
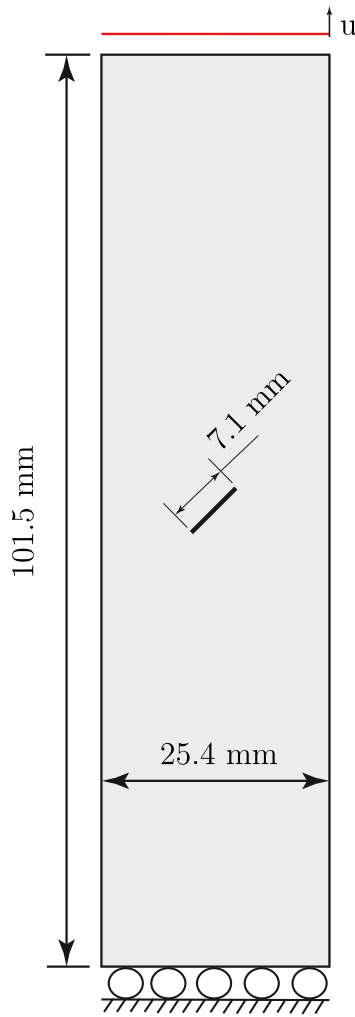
Fig. 23. Inclined center crack specimen geometry. Width of the inclined crack is 0.2 mm and the inclination angle is 45°. Bottom of the specimen is restrained against *y*-direction and one node at the middle is restrained against *x*-direction. Uniform displacement is applied on the top.

and

$$2(1 - \beta)(1 - \phi)\Psi_0 = \frac{\mathcal{G}_c}{l}(\phi - l^2 \nabla \cdot \nabla \phi) + \alpha \dot{\phi} \quad \text{in} \quad \Omega_0. \tag{30}$$

with boundary conditions

$$\boldsymbol{P} \cdot \boldsymbol{N} = \boldsymbol{T} \quad \text{on} \quad \partial \Omega_0^T, \tag{31}$$

$$\boldsymbol{u} = \bar{\boldsymbol{u}} \quad \text{on} \, \partial \Omega_{0,u}, \tag{32}$$

$$\nabla \phi \cdot \boldsymbol{N} = 0 \quad on \quad \partial \Omega_0. \tag{33}$$

4.2. Hybrid phase field model

The expression (Ψ_0) in Eq. (30) refers to the total strain energy in the material. To ensure that the crack occurs only in the tensile region of the material, it is necessary to determine the active part of the energy that is truly responsible for crack evolution. Here, we follow the hybrid (isotropic–anisotropic type) formulation (Ambati et al., 2015) where the total elastic stiffness is degraded but only the active part of strain energy (Ψ_0^{act}) will be used for solving the phase field equation. The equations pertaining to various phase field formulations are given below.

4.2.1. Isotropic formulation

In this case, the total strain energy contributed from the active as well as the passive part is used for the crack formation. In this case, the total stress tensor is degraded due to fracture. Mathematically,

$$\boldsymbol{P}(\boldsymbol{F}, \phi) = g(\phi)\frac{\partial \Psi_0}{\partial \boldsymbol{F}} \quad \text{and} \quad 2(1 - \beta)(1 - \phi)\Psi_0 = \frac{\mathcal{G}_c}{l}(\phi - l^2 \Delta \phi) + \alpha \dot{\phi} \quad (34)$$

4.2.2. Tension–compression asymmetry formulation

Here, only the tensile part of the stress tensor is degraded and active part of strain energy takes part is used in the crack formation. This prevents crack in the compressive region.

$$\boldsymbol{P}(\boldsymbol{F}, \phi) = g(\phi)\frac{\partial \Psi_0^{act}}{\partial \boldsymbol{F}} + \frac{\partial \Psi_0^{pas}}{\partial \boldsymbol{F}} \quad \text{and} \quad 2(1-\beta)(1-\phi)\Psi_0^{act} = \frac{\mathcal{G}_c}{l}(\phi - l^2 \Delta \phi) + \alpha \dot{\phi}$$

$$(35)$$

4.2.3. Hybrid formulation

The definition of stress and the governing evolution equation in this case are

$$\boldsymbol{P}(\boldsymbol{F}, \phi) = g(\phi)\frac{\partial \Psi_0}{\partial \boldsymbol{F}} \quad \text{and} \quad 2(1 - \beta)(1 - \phi)\Psi_0^{act} = \frac{\mathcal{G}_c}{l}(\phi - l^2 \Delta \phi) + \alpha \dot{\phi} \quad (36)$$

The advantage of the hybrid approach is that it avoids the complex numerical treatment of nonlinear Eq. (35)(a) and uses Eq. (34)(a) for stress calculations. But it considers the active part of strain energy to solve the crack phase field. To avoid the crack to heal, the strain energy in the region is assessed in the whole time range [0, $\mathcal{T}$] and stored as a history parameter which is defined as follows.

$$\mathcal{H}^+_{t \in [0, \mathcal{T}]} = \text{Max}(\Psi_0^{act}(\lambda_i^+, J, t)). \tag{37}$$

Definition of λ_i^+ is based on critical stretches which are given in the next section.

4.3. Additive decomposition of strain energy density based on critical stretch

To find the crack initiation criteria based on the critical principal stretches, we define the active part of strain energy by additive decomposition. A neo-Hookean type strain energy density function of the form given below is considered (Miehe and Schänzel, 2014).

$$\Psi_0(\boldsymbol{F}) = \frac{\mu}{2}\left[\boldsymbol{F} : \boldsymbol{F} - 3\right] + \frac{\mu}{\eta}[J^{-\eta} - 1], \quad \eta = \frac{2\nu}{1 - 2\nu} \; . \tag{38}$$

Here μ is the shear modulus and ν is the Poisson's ratio of the material in the small strain regime. To begin with the energy decomposition, we express the energy density function in deviatoric and volumetric form.

$$\Psi_0 = \Psi_0^{dev}(\lambda_1, \lambda_2, \lambda_3) + \Psi_0^{vol}(J). \tag{39}$$

$$\Psi_0^{dev}(\lambda_1, \lambda_2, \lambda_3) = \frac{\mu}{2}\sum_{i=1}^{3}(\lambda_i^2 - 1), \quad \Psi_0^{vol}(J) = \frac{\mu}{\eta}[J^{-\eta} - 1], \quad J = \lambda_1 \lambda_2 \lambda_3.$$

$$(40)$$

Although Ψ_0^{vol} expression does not become exactly zero for $J = 1$, the value is nearly equal to zero for this definition of volumetric energy. Here, λ_i are the principal stretches which are square roots of eigen values of Right Cauchy Green deformation tensor $\boldsymbol{C}$. The active and passive parts of energy are computed based on tensile and compressive nature of λ_i and on the nature of the volumetric deformation. This combination of deviatoric and volumetric energy for defining active and passive part are expressed as (See Fig. 7, 8),

$$\Psi_0^{act} = \Psi_0^{dev}(\lambda_i^+) + X, \tag{41}$$

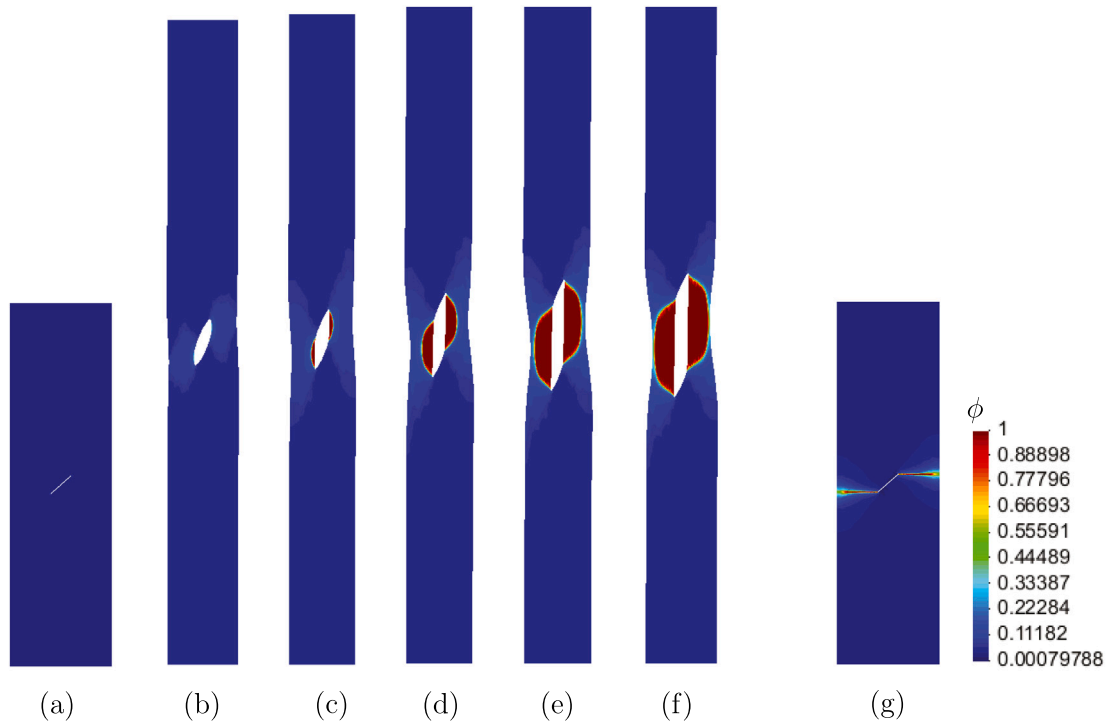$$\Psi_0^{pas} = \Psi_0^{dev}(\lambda_i^-) + Y. \tag{42}$$

Fig. 24. Crack pattern at the displacement of (a) $u = 0$ mm or undeformed state, (b) $u = 65.38$ mm, (c) $u = 68.98$ mm, (d) $u = 70.18$ mm, (e) $u = 70.58$ mm, (f) $u = 70.66$ mm applied for length scale $l = 0.1$ mm and smallest element size of 0.04 mm. (g) Crack pattern in the reference configuration.
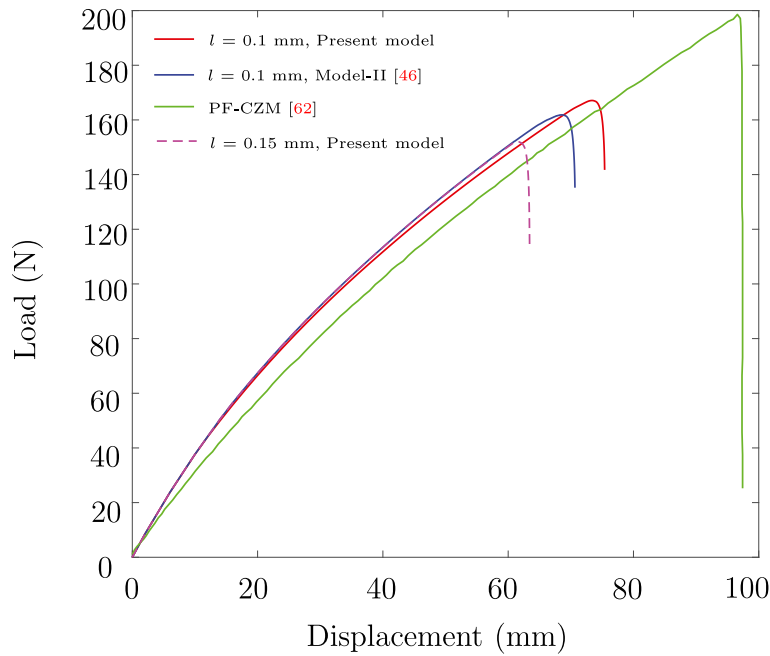

Fig. 25. Comparison of load displacement plot for centrally inclined crack specimen with initial edge crack length of 7 mm for different length scale. Smallest element size of 0.04 mm in-front of the crack tip is considered. Critical stretch $\lambda_{cr} = 1.79$ is used.

Where, the fracture contributing stretches (λ_i^+) and passive stretches (λ_i^-) are defined as

$$\lambda_i^+ = \begin{cases} \lambda_i & \text{if } \lambda_i \geq \lambda_{cr}. \\ 1 & \text{if } \lambda_i < \lambda_{cr}. \end{cases} \quad \text{and} \quad \lambda_i^- = \begin{cases} 1 & \text{if } \lambda_i \geq \lambda_{cr}. \\ \lambda_i & \text{if } \lambda_i < \lambda_{cr}. \end{cases} \quad (43)$$

and the definition of X and Y is,

$$X = \Psi_0^{vol}(J) \text{ and } Y = 0, \quad \text{if } J \geq 1,$$
$$X = 0 \text{ and } Y = \Psi_0^{vol}(J), \quad \text{if } J < 1. \quad (44)$$

Above Eq. (43) ensures that the individual principal stretches contribute to the active part of energy if and only if their value is more than λ_{cr}. This is because $\lambda_i^+ = 1$, if $\lambda_i < \lambda_{cr}$. $\lambda_i^+ = 1$ makes the deviatoric
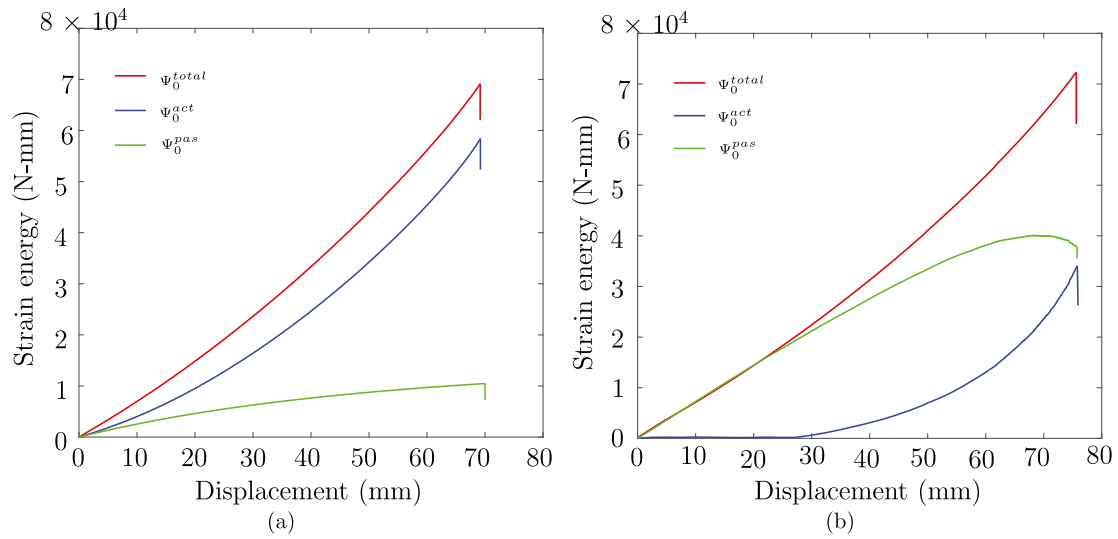
Fig. 26. Plot of active energy, passive energy and total energy in centrally inclined crack specimen.(a) Energy decomposition without critical stretch. (b) Present model for length scale $l = 0.1$ mm, Critical stretch $\lambda_{cr} = 1.79$.
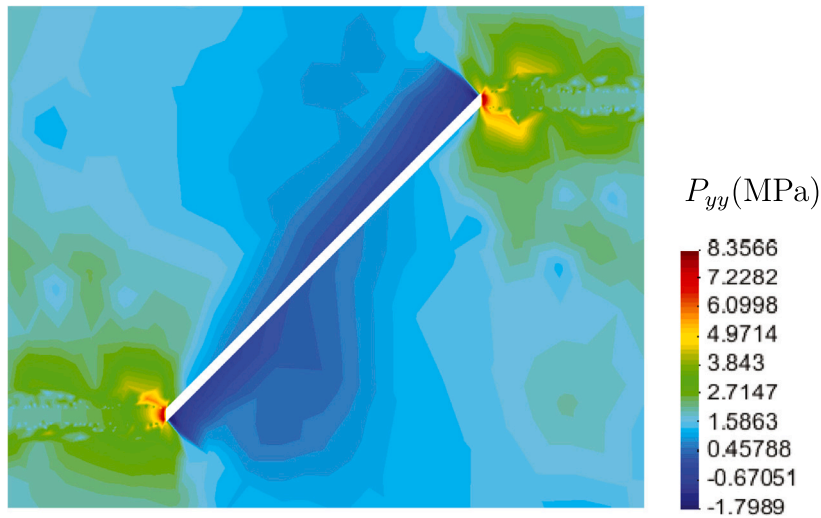

Fig. 27. Principal stress plot in inclined center crack specimen just before crack initiation load value $F = 90$ N (Pidaparti et al., 1990).

part of energy in Eq. (40)) to be zero for that particular principal stretch. This ensures the crack phase-field remains zero (undamaged state) even under material deformation. Hence this method guarantees a threshold energy value for the crack initiation. This proposed method of energy decomposition matches with the definition of tensile and compressive stretch given in Tang et al. (2019), if we take $\lambda_{cr} = 1$ in Eq. (43). Eq. (44) states that in the case of compression ($J < 1$) there is no contribution from the volumetric part of energy towards the crack formation. Cracks form only in volumetric tension ($J \geq 1$).

According to the above definition, if one of the principal stretches is greater than λ_{cr} and the other two are less than it, then the stretch which is greater than λ_{cr} only contributes to the active part of strain energy and other two contribute to the passive part. Similarly, if the volume increases ($J > 1$), it contributes to the active part of strain energy otherwise it contributes to the passive part. The absolute value of all energy measures is plotted for each numerical study.

Numerical examples in Section 5 are based on styrene-butadiene rubber (SBR). For mode-I fracture, we have adopted the final rupture tensile stretch $\lambda_{tensile} = 2.65$ for this material from experimental observation (see Figure 4 in Hocine et al. (2002) for SBR). The stretch is measured by the ratio of deformed length to the undeformed length

between two marking lines equally spaced (10 mm) from the center of the specimen (Fig. 9(b)) in the experiment. Eq. (3) is used to arrive at the critical stretch value (λ_{cr}). For the mixed mode fracture case, we have taken the tensile test conducted by Pidaparti et al. (1990). The test specimen is shown in Fig. 9(a). The rupture tensile stretch ($\lambda_{tensile}$) depends on the properties of the SBR specimen and can vary from 1.8 to 2.9 (see curve D of Figure 2 in Pidaparti et al., 1990).

The specimen geometry and thickness may affect the rupture tensile stretch. The effect of geometry and thickness on rupture tensile stretch value is not studied here. The size of the experimental setup from the literature and the numerical examples presented here are of the same order or similar in size. Hence, the same rupture tensile stretch is considered for the calculation of critical stretch. For mixed-mode fracture, the strong assumption of $\lambda_2 = \lambda_3$ can be relaxed to obtain a more accurate value of critical stretch. The rupture tensile stretch used here is measured when there is no pre-defined notch in the specimen. But, this value might differ depending on the position, orientation, and extent of the initial crack in the specimen. The dependence of λ_{cr} on the extent of deformation, the distribution of stresses, and other factors discussed above can be considered an extension of this work.
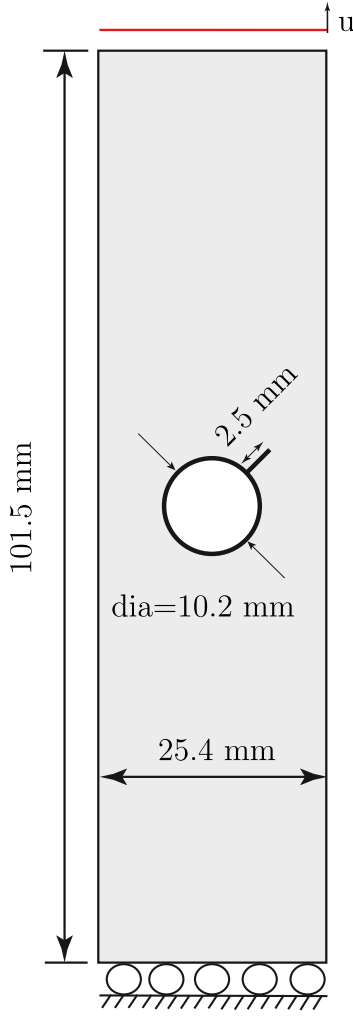
Fig. 28. Circular hole with inclined crack specimen geometry. Width of the inclined crack is 0.2 mm and the inclination angle is 45°. Bottom of the specimen is restrained against *y*-direction and one node at the middle is restrained against *x*-direction.

We assume that λ_{cr} to be constant throughout the simulation for all material points.

4.4. Finite element formulation

For the finite element framework, we find the weak form of the governing equations by multiplying admissible test function $\boldsymbol{w}_u$ for deformation field and w_ϕ for phase field and integrate over the domain.

Neglecting the traction and body force, the residual for the deformation field is obtained as follows

$$\boldsymbol{R}_\varphi = \int_{\Omega_0} \boldsymbol{P} : \nabla_X \boldsymbol{w}_u \, d\Omega_0 = 0. \tag{45}$$

$$\boldsymbol{R}_\phi = \int_{\Omega_0} \Big[w_\phi \frac{\mathcal{G}_c}{l} \phi + w_\phi \mathcal{G}_c l \nabla \phi \cdot \nabla w_\phi$$

$$- 2(1 - \beta)(1 - \phi)\Psi_0^{act} w_\phi + w_\phi \alpha \frac{(\phi - \phi_{n-1})}{\Delta t} \Big] d\Omega_0 = 0.$$

4.4.1. Discretization of field variables

The deformation map and the weight functions used in the FEM discretization at the element level are given by

$$\boldsymbol{\varphi}(\boldsymbol{X}) \approx \sum_{j=1}^{node} \boldsymbol{\varphi}^j N^j(\boldsymbol{X}), \quad \phi \approx \sum_{j=1}^{node} \phi^j N^j(\boldsymbol{X}). \tag{46}$$

and

$$\boldsymbol{w}_u = N^i(\boldsymbol{X}), \quad w_\phi = N^i(\boldsymbol{X}). \tag{47}$$

The gradient of weight function is approximated as

$$\nabla_X \boldsymbol{w}_u = \nabla_X N^i(\boldsymbol{X}). \tag{48}$$

After putting approximation to the residual, we have

$$\boldsymbol{R}_\varphi^i = \int_{\Omega_0} \boldsymbol{P} \cdot \nabla_X N^i d\Omega_0 = 0. \tag{49}$$

$$\boldsymbol{R}_\phi^i = \int_{\Omega_0} \Big[\frac{\mathcal{G}_c \phi}{l} N^i + \mathcal{G}_c l(\nabla_X \phi \cdot \nabla_X N^i)$$

$$- 2(1 - \beta)(1 - \phi)\mathcal{H}^+ N^i + N^i \alpha \frac{(\phi - \phi_{n-1})}{\Delta t} \Big] d\Omega_0 = 0. \tag{50}$$

4.4.2. Tangent operators and stiffness terms

The linearized tangent stiffness terms are given below.

$$\boldsymbol{K}_{\varphi\varphi}^{ij} = \frac{\partial \boldsymbol{R}_\varphi^i}{\partial \varphi_j} = \int_{\Omega_0} \Big[\Big[\frac{\partial \boldsymbol{P}}{\partial \boldsymbol{F}} \cdot \nabla_X N^i \Big] \cdot \nabla_X N^j \Big] d\Omega_0, \tag{51}$$

and

$$\boldsymbol{K}_{\phi\phi}^{ij} = \int_{\Omega_0} \Big[\frac{\mathcal{G}_c}{l} N^i \cdot N^j + \mathcal{G}_c l(\nabla_X N^i \cdot \nabla_X N^j) + 2\mathcal{H}^+(1 - \beta)N^i \cdot N^j +$$

$$\frac{\alpha}{\Delta t} N^i \cdot N^j \Big] d\Omega_0. \tag{52}$$

Driving force for damage is obtained as

$$F_\phi^i = \int_{\Omega_0} 2(1 - \beta)\mathcal{H}^+ \cdot N^i + \alpha \frac{\phi_{n-1}}{\Delta t} \cdot N^i d\Omega_0. \tag{53}$$

The expressions for the first Piola Kirchhoff stress $\boldsymbol{P}$ and tangent operators $\frac{\partial \boldsymbol{P}}{\partial \boldsymbol{F}}$ are given below.

$$\boldsymbol{P} = \frac{\partial \Psi_0}{\partial \boldsymbol{F}} = \boldsymbol{P}_1 + \boldsymbol{P}_2. \tag{54}$$

$$(P_1)_{ij} = \mu F_{ij}, \tag{55}$$

$$(P_2)_{ij} = -\mu J^{-\eta} F_{ji}^{-1}. \tag{56}$$

$\boldsymbol{P}_1$ and $\boldsymbol{P}_2$ represents the deviatoric and volumetric part of First Piola–Kirchhoff stress tensor $\boldsymbol{P}$ respectively. The linearized tangent stiffness terms are written as follows

$$\mathbb{A}_{ijkl}^1 = \frac{\partial (P_1)_{ij}}{\partial F_{kl}} = \mu \delta_{ik} \delta_{jl}, \tag{57}$$

$$\mathbb{A}_{ijkl}^2 = \frac{\partial (P_2)_{ij}}{\partial F_{kl}} = \mu [\eta J^{-\eta} F_{lk}^{-1} F_{ji}^{-1} + J^{-\eta} F_{jk}^{-1} F_{il}^{-1}]. \tag{58}$$

4.5. Numerical implementation

Mechanical problem (Eq. (29)) coupled with evolution equation (Eq. (30)) is solved using a staggered approach, where the phase field is kept frozen while solving for the displacement field, and the displacement field is kept constant while solving for the phase field. History parameter $\mathcal{H}^+$, which stores the maximum active strain energy up to the current displacement/load step links the two sub-problems, and is responsible for fracture evolution. The flowchart showing the procedure of the staggered scheme is given in Fig. 10.

Consider $(r + 1)$th iteration of nth load step in the simulation. Applying the Newton–Raphson method to solve for deformation field ($\boldsymbol{\varphi}$), we have

$$\delta \boldsymbol{u} = -[\boldsymbol{K}_{\varphi\varphi}(\boldsymbol{u}_n^r)]^{-1} \boldsymbol{R}_{\varphi,n}^r. \tag{59}$$

Where, $\boldsymbol{K}_{\varphi\varphi}(\boldsymbol{u}_n^r) = \Big[\frac{\partial \boldsymbol{R}_\varphi}{\partial \boldsymbol{\varphi}} \Big]_n^r$ as per Eq. (51)

Expression for $\boldsymbol{R}_\varphi$ is given as per Eq. (49), $\boldsymbol{u}_n^{r+1} = \boldsymbol{u}_n^r + \delta \boldsymbol{u}$.
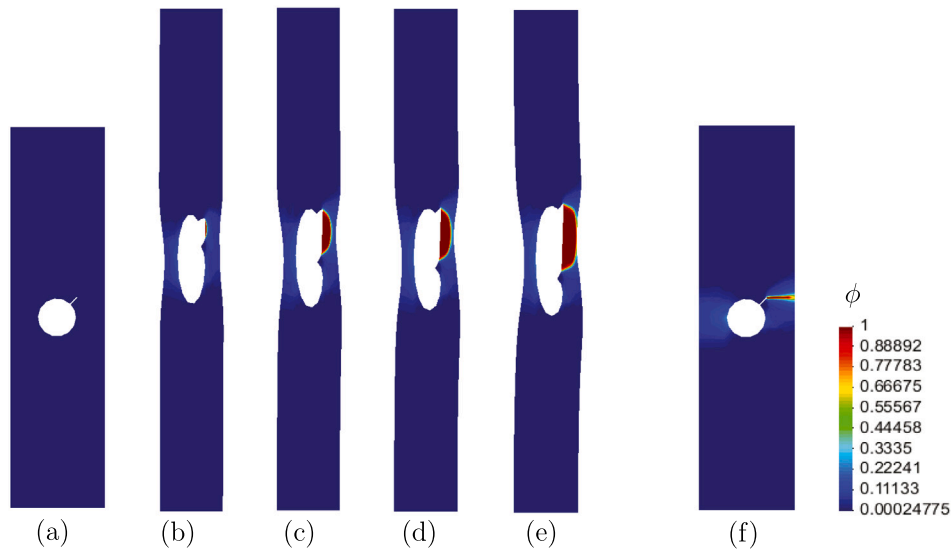
Fig. 29. Crack pattern at the displacement of (a) $u = 0$ mm or undeformed state, (b) $u = 50.6$ mm, (c) $u = 52$ mm, (d) $u = 52.1$ mm, (e) $u = 52.2$ mm (f) Crack pattern in the reference configuration. Length scale $l = 0.15$ mm is used.
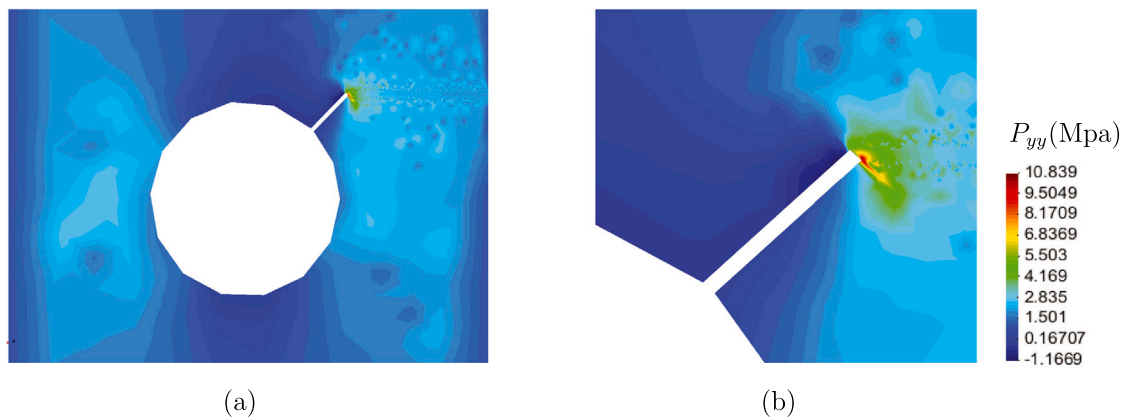

Fig. 30. Principal stress plot in circular hole with inclined crack specimen just before crack initiation load value $F = 90$ N (Pidaparti et al., 1990) (a) Near to the hole region (b) Near to the crack tip.

Solving for phase-field (ϕ) in $[\boldsymbol{K}_{\phi\phi}] \cdot \{\boldsymbol{\phi}\} = \{\boldsymbol{F}_\phi\}$ is carried out in a single step (without any iteration) as $\boldsymbol{K}_{\phi\phi}$ does not involve any non-linear terms. λ, μ are the Lame's parameters. The tolerance (Tol) is taken as 10^{-7} for each simulation and the maximum number of iterations (r_{max}) within one load step is considered as 25 for convergence. $\mathcal{R}_\varphi$ is the $L2$-norm of the residual vector $\boldsymbol{R}_\varphi$. n_{max} is the maximum number of load steps and n is the current load step. The simulations are carried out using MATLAB and the figures showing crack patterns are plotted using GiD software.

5. Numerical results and discussions

5.1. Double edge notched specimen in tension (DENT) test

The experimental work of Hocine et al. (2002) on double edge notch in tension (DENT) test of styrene-butadiene rubber (SBR) is used as a benchmark example for the nearly incompressible problem. The geometry and boundary conditions are given in Fig. 11. The notch width is 0.5 mm. The Lamé constants are $\mu = 0.203$ MPa and $\lambda = 1.827$ MPa with Poisson's ratio $\nu = 0.45$. The critical fracture energy $\mathcal{G}_c$ (=2.67 N/mm) is considered according to the polymer network model (see Miehe and

Schänzel, 2014). The thickness of the specimen in the experiments is 3 mm. Exploiting the symmetry of the specimen, we have analyzed only the right half portion of the specimen and is discretized into 6645 quadrilateral elements with 8 elements in the initial notch width resulting smallest element size of 0.0625 mm. Length scale $l = 1$ mm is considered. Comparatively larger increment value is used until the total displacement of 38 mm and then the displacement increment (Δu) of 0.01 is used during the crack propagation. From the uniaxial test of SBR specimen, it is found that the rupture tensile stretch ($\lambda_{tensile}$) is approximately 2.65 (see Figure 4 in Hocine et al., 2002 for SBR). The critical stretch λ_{cr} (=1.61) is evaluated using Eq. (3). The crack patterns are shown in Fig. 12.

The present study predicts almost the same peak load as compared to the experimental observation by Hocine et al. (2002). The energy decomposition without critical stretch predicts a little lesser peak load although the failure displacements are the same (see Fig. 13(a)). The length scale of $l = 1$ mm admits good agreement with experiments. Higher length scale values predict lesser peak load compared to lower length scale (see Fig. 13(b)). From Fig. 15(b), it is observed that active energy is almost zero up to a certain displacement due to the use of critical stretch for energy decomposition. Beyond this point,
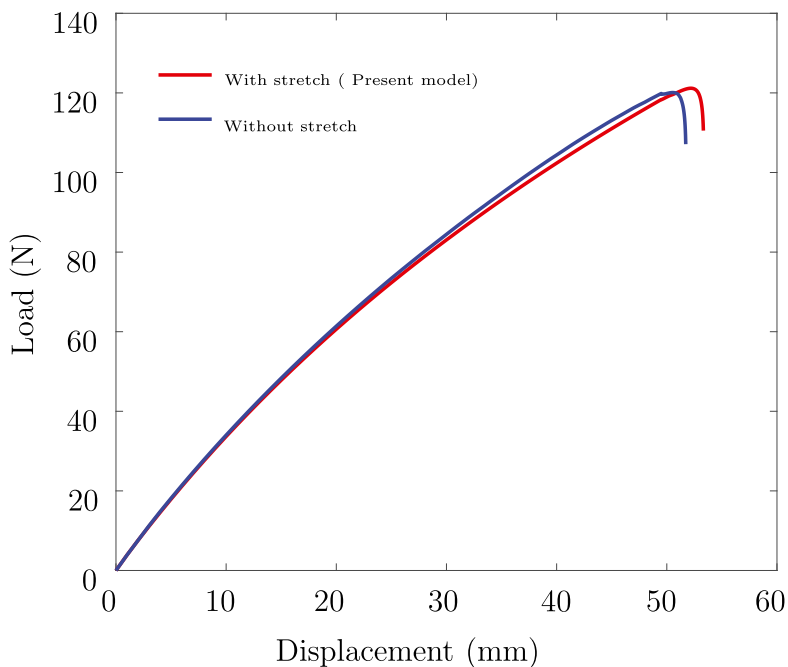
Fig. 31. Load displacement plot for circular hole with inclined crack specimen using length scale l = 0.15 mm with stretch (λ_{cr} = 1.79) and without using stretch criteria.
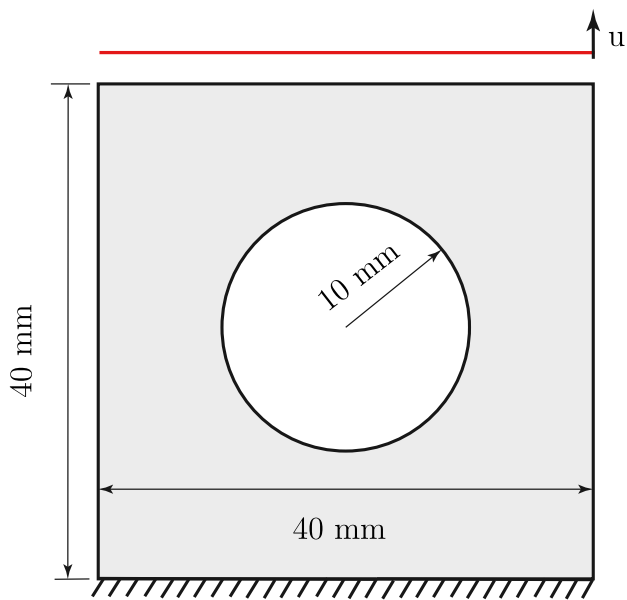

Fig. 32. Geometry of plate with a central hole. Bottom end is fixed and uniform load is applied on the top.

active energy increases and contributes to crack propagation. When the condition of stretch is used, active energy is almost equal to the total energy indicating the complete use of energy during crack evolution, whereas some residual energy is remaining when this condition is not used (Fig. 15(a)). For a* = 28 mm, the displacement at which the crack initiates is almost same as per the present model and by the other PF model. Hence, the crack pattern would be same for both the cases. Crack initiates little early in case of a* = 12 mm as per the present study. Comparison for crack evolution are shown in Fig. 14. Because of the rapid progression, substantial crack growth at displacement of u =

62.75 mm has already happened in the present model while it is just starting according to the other.

The effect of reduction in $\mathcal{G}_c$ values on failure load and displacement is studied. $\mathcal{G}_c$ is varied from 2.67 to 2.5, 2.2 (Fig. 17) at all material points by varying different values of ω_2, if the stretch is more than λ_{cr}. The average value of $\mathcal{G}_c$ in the crack tip (0.3 mm $\times$ 0.3 mm square red block) as shown in Fig. 16(b) is used for plotting the reduced value of critical fracture toughness $\mathcal{G}_{rd}$ in Fig. 16(a). The peak load decreases as the $\mathcal{G}_c$ reduced to lower values. Due to lower $\mathcal{G}_c$, less energy is required to propagate the crack and causes the material to fail early.

The crack evolution follows the same pattern for different degraded values of critical fracture toughness, but the crack initiation point differs for each as per Fig. 17. At the displacement of 40 mm, the crack has already propagated substantially when $\mathcal{G}_c$ degraded to 2.2 N/mm. But at the same displacement value, crack is just initiating when $\mathcal{G}_c$ is not degraded and the crack front is little more damaged when $\mathcal{G}_c$ is degraded to 2.5 N/mm from 2.6 N/mm. The crack patterns are shown in Fig. 18. Energy decomposition with critical stretch increases the peak load while degradation of $\mathcal{G}_c$ decreases the failure displacement.

5.2. Penny shaped precracked test specimen

The benchmark example of a penny-shaped pre-crack specimen is considered as shown in Fig. 19. The height and width of the specimen are 0.4 mm and 2 mm respectively. A central notch of length 0.2 mm and width of 0.005 mm is modeled to introduce a small perturbation in the system. A constant incremental displacement (Δu) of 0.01 mm is applied until a total displacement of 0.38 mm and is reduced to 0.0001 mm during the crack propagation. The domain is discretized into 5000 quadrilateral elements. Elastic properties λ, μ of the material are taken as 45 MPa and 5 MPa respectively with Poisson's ratio ν = 0.45 to consider weak compressibility. Critical energy release rate $\mathcal{G}_c$ is taken as 2.4 N/mm and critical stretch value is taken the same as per the previous example i.e. λ_{cr} = 1.61. The analysis is carried out for length scales l = 0.01 mm and l = 0.02 mm to study the effect of length scales. The crack patterns are shown in Fig. 20. The load–displacement curve is shown in Fig. 21. The present study predicts a higher peak
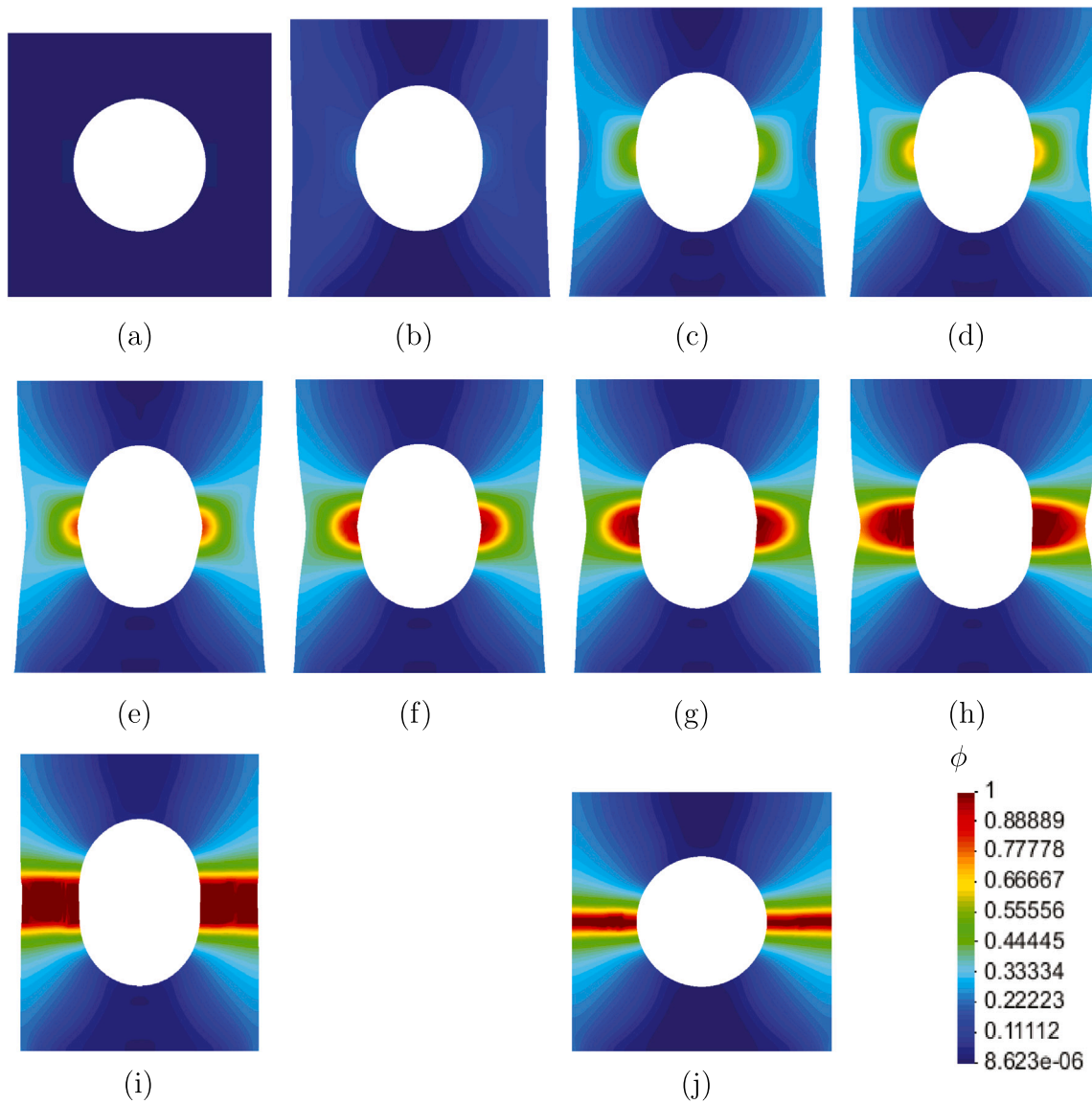
Fig. 33. Crack pattern at the displacement of (a) $u = 0$ mm or undeformed state (b) $u = 2.08$ mm (c) $u = 4.48$ mm (d) $u = 4.88$ mm (e) $u = 5.08$ mm (f) $u = 5.28$ mm (g) $u = 5.38$ mm (h) $u = 5.48$ mm (i) $u = 5.68$ mm applied for length scale $l = 1.6$ mm. (j) Crack pattern in the reference configuration. The geometry is discretized with uniform element size of 0.5 mm. and Poisson's ratio $v = 0.42$ is considered for this simulation.

load compared to Miehe and Schänzel (2014). The displacement for final rupture is also more. As the artificial viscosity parameter (α) is one type of regularization used for the rate-independent case, the load–displacement plot approaches the rate-independent limit as a lesser value of α is used. Higher the viscosity parameter, the higher the failure displacement, although the peak load is almost the same. The energy plot given in Fig. 22 shows that active energy increases gradually until fracture initiates and then drops afterward. When the critical stretch criteria are used, the active energy is almost zero up to a certain stretch value and gradually increases afterward (Fig. 22(b)). Present model predicts relatively higher displacement values at crack initiation than other model. Hence, the damage pattern will follow the same as per other PF models, but the crack initiation point would differ.

5.3. Mixed mode fracture in inclined center crack specimen

To verify the present model for mixed mode fracture, the experimental work of Pidaparti et al. (1990) on the inclined center crack specimen is considered. The geometry and the boundary conditions are

given in Fig. 23. Critical fracture energy $\mathcal{G}_c = 15$ N/mm (Range of 12.5 N/mm-24.5 N/mm in Pidaparti et al. (1990)), Young's modulus $E = 6.5$ MPa and Poisson's ratio $v = 0.45$ are taken for the simulation as given in Mandal et al. (2020). Plane stress condition is considered. Critical stretch value $\lambda_{cr} = 1.79$ is adopted based on the tensile stretch value $\lambda_{tensile} = 2.9$ (see curve D of Figure 2 in Pidaparti et al. (1990)). Simulations are performed for two different length scales $l = 0.1$ mm and $l = 0.15$ mm. The crack patterns are shown in Fig. 24.

The experimental range for crack initiation load is reported as (180–234) N (Pidaparti et al., 1990). The present study predicts the peak load of 167 N (Fig. 25) for length scale $l = 0.1$ mm. The lower length scale predicts a higher peak load than the higher length scale value. The active energy plot shows that up to 26 mm displacement there is little energy contribution towards the crack formation and afterward, the active energy increases continuously (Fig. 26(b)). Active energy contributes to fracture from the beginning of loading if there is no definition for active energy based on stretch (Fig. 26(a)). The principal
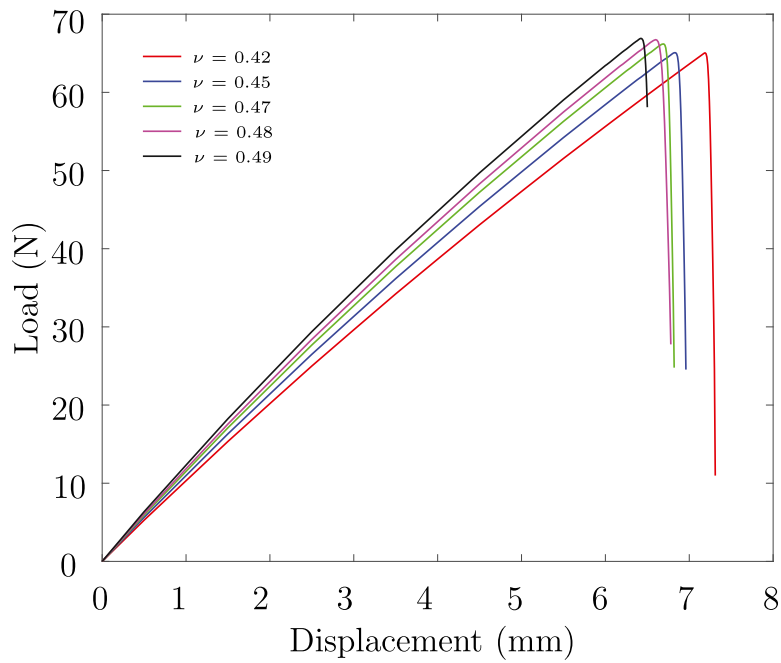
Fig. 34. Load vs Displacement plot of plate with a central hole example for different Poisson's ratio. Length scale l = 1.6 mm with minimum element size of 0.2 mm is adopted.
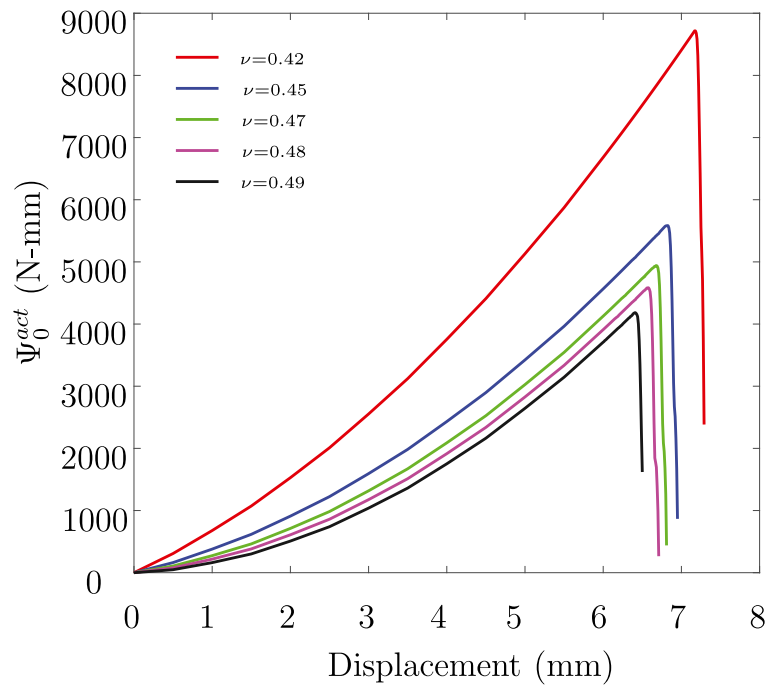

Fig. 35. Active energy plot for different Poisson's ratio attaining incompressible limit.

stress plot agrees well with Pidaparti et al. (1990) and is shown in Fig. 27.

5.4. Circular hole with inclined crack specimen

This example is also a case of mixed mode fracture condition with unsymmetric stress concentration. The geometry and boundary condition is given in Fig. 28. The material parameter is taken the same as the CINT specimen. The crack pattern is shown in Fig. 29. The stress plot agrees well with the work of Pidaparti et al. (1990) and is shown in

Fig. 30. This study predicts the failure load to be 120 N (Fig. 31) when length scale l = 0.15 is used, and the experimental range is (120–169) N. The lower length scale (l) predicts a higher failure load, which is related to the material parameter.

5.5. Fracture in plate with a central hole under uniaxial tension

This example is considered to study the effect of Poison's ratio on fracture behavior. The geometry and the boundary conditions of a square plate with a central hole are given in Fig. 32. The critical

fracture energy G_c = 4 N/mm, shear modulus μ = 5 MPa are taken for the simulation. Plane strain condition is assumed. The crack patterns and the load–displacement curve are shown in Fig. 33 and Fig. 34 respectively. As the Poisson's ratio approaches the incompressible limit, the peak load increases, and the failure displacement decreases. Contribution of active energy to the fracture increases as the Poisson's ratio decreases shown in Fig. 35.

6. Conclusions

A new energy decomposition method is proposed specifically for rubber-like polymers to model fracture using phase field method in mode-I and for mixed mode (I/II) case. A threshold value of stretch or critical stretch is evaluated from tensile test experimental data presented in literature. By considering material to be nearly incompressible, expression for critical stretch in terms of multiaxial stretch values is obtained. This is used to establish a criteria for crack initiation. Different numerical examples are studied to validate the present model. Considering the Lake-Thomas model of the critical fracture energy of polymer, we propose a exponential reduction of G_c, only beyond the critical value of stretch. This is assumed considering reduced number of elastically effective polymer chains per unit volume due to the effect of damage. As the degradation of elastic energy does not happen unless it reaches a certain value, this model predicts comparatively larger peak loads before the final fracture as compared to standard phase field models. Crack patterns at various instances are plotted and it is inferred that the crack grows faster after initiation and requires small displacement increments. Fracture modeling in the mixed-mode case is more sensitive to the length scale than mode-I case. As the length scale l is related to the material properties, determination of its value is essential for predicting correct value of failure load using PFM. The effect of reduction in G_c value for various ranges is analyzed based on stretch. The percentage of reduction can be attributed to the nature of polymer chains and its weakening response to the stretch. Present model with degradation of G_c predicts crack initiation earlier than when G_c is not degraded. The effect of Poisson's ratio is studied and it is inferred that, the positive energy contribution towards fracture energy increases as the Poisson's ratio decreases. The difference between total and active energy reduces with the increase in Poisson's ratio, while keeping the other parameters constant.

CRediT authorship contribution statement

P. Aurojyoti: Conceptualization, Methodology, Software, Formal analysis, Writing – original draft. **A. Rajagopal:** Supervision, Conceptualization, Formal analysis, Writing – review & editing. **K.S.S. Reddy:** Software, Writing – editing.

Declaration of competing interest

The authors declare that they have no known competing financial interests or personal relationships that could have appeared to influence the work reported in this paper.

Data availability

Data will be made available on request.

References

Akagi, Y., Sakurai, H., Gong, J.P., Chung, U., Sakai, T., 2013. Fracture energy of polymer gels with controlled network structures. J. Chem. Phys. 139 (14), 144905.

Ambati, M., Gerasimov, T., Lorenzis, L.D., 2015. A review on phase-field models of brittle fracture and a new fast hybrid formulation. Comput. Mech. 55 (2), 383–405.

Ambati, M., Kruse, R., Lorenzis, L.D., 2016. A phase-field model for ductile fracture at finite strains and its experimental verification. Comput. Mech. 57, 149–167.

Ang, I., Bouklas, N., Li, B., 2022. Stabilized formulation for phase-field fracture in nearly incompressible hyperelasticity. Internat. J. Numer. Methods Engrg. 123 (19), 4655–4673.

Arash, B., Exner, W., Rolfes, R., 2021. A finite deformation phase-field fracture model for the thermo-viscoelastic analysis of polymer nanocomposites. Comput. Methods Appl. Mech. Engrg. 381, 113821.

Arruda, E.M., Boyce, M.C., 1993. A three-dimensional constitutive model for the large stretch behavior of rubber elastic materials. J. Mech. Phys. Solids 41 (2), 389–412.

Ayatollahi, M.R., Heydari-Meybodi, M., Dehghany, M., Berto, F., 2016. A new criterion for rupture assessment of rubber-like materials under mode-I crack loading: The effective stretch criterion. Adv. Eng. Mater. 18 (8), 1364–1370.

Barba, D., Arias, A., Garcia-Gonzalez, D., 2020. Temperature and strain rate dependences on hardening and softening behaviours in semi-crystalline polymers: Application to PEEK. Int. J. Solids Struct. 182–183, 205–217.

Basak, A., Rajagopal, A., Basappa, U., Hossain, M., 2021. The use of contravariant tensors to model anisotropic soft tissues. Int. J. Appl. Mech. 13 (03), 2150039.

Borden, M.J., Hughes, T.J.R., Landis, C.M., Anvari, A., Lee, I.J., 2016. A phase-field formulation for fracture in ductile materials: Finite deformation balance law derivation, plastic degradation, and stress triaxiality effects. Comput. Methods Appl. Mech. Engrg. 312, 130–166.

Borden, M.J., Verhoosel, C.V., Scott, M.A., Hughes, T.J.R., Landis, C.M., 2012. A phase-field description of dynamic brittle fracture. Comput. Methods Appl. Mech. Engrg. 217–220, 77–95.

Bourdin, B., Francfort, G.A., Marigo, J.-J., 2000. Numerical experiments in revisited brittle fracture. J. Mech. Phys. Solids 48 (4), 797–826.

Boyce, M.C., Arruda, E.M., 2000. Constitutive models of rubber elasticity: A review. Rubber Chem. Technol. 73 (3), 504–523.

Caimmi, F., Roberto, C., Francesco, B.V., Claudia, M., Marta, R., 2015. Toughness of natural rubber compounds under biaxial loading. Eng. Fract. Mech. 149, 250–261.

Coveney, V.A., 2006. Elastomers and Components: Service Life Prediction-Progress and Challenges. Woodhead Publishing.

Dal, H., Kemal, A., Badienia, Y., 2021. On the performance of isotropic hyperelastic constitutive models for rubber-like materials: A state of the art review. Appl. Mech. Rev. 73 (2), 020802.

Denli, F.A., Gültekin, O., Holzapfel, G.A., Dal, H., 2020. A phase-field model for fracture of unidirectional fiber-reinforced polymer matrix composites. Comput. Mech. 65 (4), 1149–1166.

Fu, X., Wang, Z., Ma, L., Zou, Z., Zhang, Q., Guan, X., 2020. Temperature-dependence of rubber hyperelasticity based on the eight-chain model. Polymers 12 (4), 932.

Gao, Y.C., 1997. Large deformation field near a crack tip in rubber-like material. Theor. Appl. Fract. Mech. 26 (3), 155–162.

Griffith, A.A., 1921. The phenomena of rupture and flow in solids. Phil. Trans. R. Soc. 221 (582–593), 163–198.

Gültekin, O., Dal, H., Holzapfel, G.A., 2018. Numerical aspects of anisotropic failure in soft biological tissues favor energy-based criteria: A rate-dependent anisotropic crack phase-field model. Comput. Methods Appl. Mech. Engrg. 331, 23–52.

Hamdi, A., Hocine, N.A., Abdelaziz, M.N., Benseddiq, N., 2007. Fracture of elastomers under static mixed mode: The strain-energy-density factor. Int. J. Fract. 144, 65–75.

He, H., Zhang, Q., Zhang, Y., Chen, J., Zhang, L., Li, F., 2022. A comparative study of 85 hyperelastic constitutive models for both unfilled rubber and highly filled rubber nanocomposite material. Nano Mater. Sci. 4 (2), 64–82.

Hesch, C., Weinberg, K., 2014. Thermodynamically consistent algorithms for a finite-deformation phase-field approach to fracture. Internat. J. Numer. Methods Engrg. 99 (12), 906–924.

Heydari-Meybodi, M., Ayatollahi, M.R., Berto, F., Yazid Yahya, M., 2019. Rupture assessment of rubber/clay nanocomposites containing a crack by means of an energy-based fracture criterion. Arch. Civ. Mech. Eng. 19 (4), 1458–1467.

Hocine, N.A., Abdelaziz, M.N., Imad, A., 2002. Fracture problems of rubbers: J-integral estimation based upon η factors and an investigation on the strain energy density distribution as a local criterion. Int. J. Fract. 117, 1–23.

Hossain, M., Steinmann, P., 2013. More hyperelastic models for rubber-like materials: consistent tangent operators and comparative study. J. Mech. Behav. Mater. 22 (1-2), 27–50.

Kolling, S., Bois, P.A.D., Benson, D.J., Feng, W.W., 2007. A tabulated formulation of hyperelasticity with rate effects and damage. Comput. Mech. 40 (5), 885–899.

Kumar, A., Francfort, G.A., Oscar, L.P., 2018. Fracture and healing of elastomers: A phase-transition theory and numerical implementation. J. Mech. Phys. Solids 112, 523–551.

Kumar, P., Steinmann, P., Mergheim, J., 2022. A graded interphase enhanced phase-field approach for modeling fracture in polymer composites. Forces Mech. 9, 100135.

Lake, G.J., Thomas, A.G., 1967. The strength of highly elastic materials. Proc. R. Soc. Lond. Ser. A 300 (1460), 108–119.

Li, B., Bouklas, N., 2020. A variational phase-field model for brittle fracture in polydisperse elastomer networks. Int. J. Solids Struct. 182–183, 193–204.

Loew, P.J., Peters, B., Beex, L.A.A., 2019. Rate-dependent phase-field damage modeling of rubber and its experimental parameter identification. J. Mech. Phys. Solids 127, 266–294.

Long, R., Krishnan, V.R., Hui, C.Y., 2011. Finite strain analysis of crack tip fields in incompressible hyperelastic solids loaded in plane stress. J. Mech. Phys. Solids 59, 672–695.

Mandal, T.K., Gupta, A., Nguyen, V.P., Rajib, C., Vaucorbeil de, A., 2020. A length scale insensitive phase field model for brittle fracture of hyperelastic solids. Eng. Fract. Mech. 236, 107196.

Mao, Y., Talamini, B., Anand, L., 2017. Rupture of polymers by chain scission. Extreme Mech. Lett. 13, 17–24.

Mi, Z., Zhang, Y., Hou, X., Wang, J., 2021. Phase field modeling of dielectric breakdown of ferroelectric polymers subjected to mechanical and electrical loadings. Int. J. Solids Struct. 217–218, 123–133.

Miehe, C., Hofacker, M., Welschinger., F., 2010. A phase field model for rate-independent crack propagation: Robust algorithmic implementation based on operator splits. Comput. Methods Appl. Mech. Engrg. 199 (45-48), 2765–2778.

Miehe, C., Schänzel, L.M., 2014. Phase field modeling of fracture in rubbery polymers. Part-i: Finite elasticity coupled with brittle failure. J. Mech. Phys. Solids 65, 93–113.

Nguyen, T.T., Yvonnet, J., Waldmann, D., He, Q.C., 2020. Implementation of a new strain split to model unilateral contact within the phase field method. Internat. J. Numer. Methods Engrg. 121 (21), 4717–4733.

Peng, F., Huang, W., Zhang, Z.Q., Guo, T.F., Ma, Y.E., 2020. Phase field simulation for fracture behavior of hyperelastic material at large deformation based on edge-based smoothed finite element method. Eng. Fract. Mech. 238, 107233.

Pidaparti, R.M.V., Yang, T.Y., Soedel, W., 1990. Plane stress finite element prediction of mixed-mode rubber fracture and experimental verification. Int. J. Fract. 45, 221–241.

Qi, Y., Calliard, J., Long, R., 2018. Fracture toughness of soft materials with rate-independent hysteresis. J. Mech. Phys. Solids 118, 341–364.

Raina, A., Miehe, C., 2015. A phase-field model for fracture in biological tissues. Biomech. Model. Mechanobiol. 15 (3), 479–496.

Russ, J., Slesarenko, V., Rudykh, S., Waisman, H., 2020. Rupture of 3D-printed hyperelastic composites: Experiments and phase field fracture modeling. J. Mech. Phys. Solids 140, 103941.

Swamynathan, S., Jobst, S., Keip, M.A., 2021. An energetically consistent tension–compression split for phase-field models of fracture at large deformations. Mech. Mater. 157, 103802.

Syao, Ouyan, Malysheva, G.V., 2014. Properties and application of rubber-based sealants. Polym. Sci. Ser. D 7 (3), 222–227.

Talamini, B., Mao, Y., Anand, L., 2018. Progressive damage and rupture in polymers. J. Mech. Phys. Solids 111, 434–457.

Tang, S., Zhang, G., Guo, T.F., Guo, X., Liu, W.K., 2019. Phase field modeling of fracture in nonlinearly elastic solids via energy decomposition. Comput. Methods Appl. Mech. Engrg. 347, 477–494.

Thamburaja, P., Sarah, K., Srinivasa, A., Reddy, J.N., 2019. Fracture of viscoelastic materials: FEM implementation of a non-local and rate form-based finite-deformation constitutive theory. Comput. Methods Appl. Mech. Engrg. 354, 871–903.

Tian, F., Zeng, J., Zhang, M., Li, L., 2022. Mixed displacement-pressure-phase field framework for finite strain fracture of nearly incompressible hyperelastic materials. Comput. Methods Appl. Mech. Engrg. 394, 114933.

Trivedi, A.R., Siviour, C.R., 2020. A simple rate-temperature dependent hyperelastic model applied to neoprene rubber. J. Dyn. Behav. Mater. 6 (3), 336–347.

Upadhyay, K., Subhash, G., Spearot, D., 2020. Visco-hyperelastic constitutive modeling of strain rate sensitive soft materials. J. Mech. Phys. Solids 135, 103777.

van Dijk, N.P., Espadas-Escalante, J.J., Isaksson, P., 2020. Strain energy density decompositions in phase-field fracture theories for orthotropy and anisotropy. Int. J. Solids Struct. 196–197, 140–153.

Volokh, Y.C., Trapper, P., 2008. Fracture toughness from the standpoint of softening hyperelasticity. J. Mech. Phys. Solids 56, 2459–2472.

Wu, P.D., Van Der Giessen, E., 1993. On improved network models for rubber elasticity and their applications to orientation hardening in glassy polymers. J. Mech. Phys. Solids 41 (3), 427–456.

Ye, J.Y., Zhang, L.W., Reddy, J.N., 2020. Large strained fracture of nearly incompressible hyperelastic materials: Enhanced assumed strain methods and energy decomposition. J. Mech. Phys. Solids 139, 103939.

Yin, B., Kaliske, M., 2020. A ductile phase-field model based on degrading the fracture toughness: Theory and implementation at small strain. Comput. Methods Appl. Mech. Engrg. 366, 113068.

Yin, B., Khodor, J., Kaliske, M., 2020a. Fracture and fatigue failure simulation of polymeric material at finite deformation by the phase-field method and the material force approach. In: Fatigue Crack Growth in Rubber Materials. 286, pp. 347–376.

Yin, B., Steinke, C., Kaliske, M., 2020b. Formulation and implementation of strain rate-dependent fracture toughness in context of the phase-field method. Internat. J. Numer. Methods Engrg. 121 (2), 233–255.

Zhang, G., Guo, T.F., Guo, X., Tang, S., Fleming, M., Liu, W.K., 2019. Fracture in tension-compression-asymmetry solids via phase field modeling. Comput. Methods Appl. Mech. Engrg. 357, 112573.

Zhou, Z., Gao, Y.C., 1998. Asymptotic character of mixed mode in plane deformation of crack in rubber-like material. Theor. Appl. Fract. Mech. 30, 225–233.